# Electrochemical properties of layered perovskite for the electrode of symmetrical solid oxide fuel cells

Yu Ri Lim[a], Harald Schlegl[b], Jeong Yun Park[a], Yu Taek Hong[a], Jin Woo Cha[a],

Chae Eun Kim[a], In Yong Kang[c], Abul Kalam Azad[d], Wonseok Choi[e],

Jung Hyun Kim[a,]*

[a] Department of Advanced Material Science and Engineering, Hanbat National University, 125, Dongseo-Daero, Yuseong-Gu, Daejeon, 34158, Republic of Korea

[b] Physics Department, Lancaster University, Bailrigg, Lancaster, LA1 4YB, United Kingdom

[c] HnPower, N9-4160, 291, Daehak-Ro, Yoseong-Gu, Daejeon, 34141, Republic of Korea

[d] Faculty of Integrated Technologies, Universiti Brunei Darussalam, Jalan Tungku Link, Gadong, BE1410, Brunei Darussalam

[e] Department of Electrical Engineering, Hanbat National University, 125, Dongseo-Daero, Yuseong-Gu, Daejeon, 34158, Republic of Korea

Corresponding author: *

Jung Hyun Kim: jhkim2011@hanbat.ac.kr, jhkim1870@gmail.com,

Tel: +82-42-821-1239, Fax: +82-42-821-1592,

Department of Advanced Materials Science and Engineering, Hanbat National University, 125, Longsoldier, Yuseong-Gu, Daejeon, 34158, Republic of Korea

## Abstract

In this study, Co free layered perovskites $SmBa(Fe_{1-x}Mn_x)_2O_{5+d}$ (SBFMn, x = 0, 0.1, 0.3 and 0.5) were proposed as candidate electrode materials for symmetrical solid oxide fuel cells (SSOFCs), and the influence of Mn/Fe ratio on electrochemical performance, electrical conductivity behavior, and structural stability was systematically investigated. Impedance measurements using LSGM based half cells showed that $SmBa(Fe_{0.9}Mn_{0.1})_2O_{5+d}$ (SBFMn 1.8-0.2) exhibited lower area specific resistance in both air and 3.9% hydrogen atmosphere, indicating balanced and enhanced oxygen reduction reaction and hydrogen oxidation reaction activity. Electrical conductivity showed that increasing Mn content led to reduced conductivity in air and nitrogen atmospheres due to weakened M-O-M orbital overlap and decreased $Fe^{4+}$ derived hole concentration. In contrast, under hydrogen atmosphere, a small degree of Mn incorporation resulted in a relative enhancement of electrical conductivity. X-ray diffraction analysis confirmed that an irreversible cubic to orthorhombic phase transition occurred exclusively under reducing conditions at approximately 450 °C, which is consistent with the conductivity decrease observed during the initial heating process and its subsequent recovery at higher temperatures. These results demonstrate that precise control of the Mn/Fe ratio enables simultaneous optimization of electrochemical activity and structural stability, providing practical design guidelines for layered perovskite electrodes in SSOFC applications.

**Keywords**: E Fuel Cells; D Perovskite; C Electrical conductivity; C Impedance

## Highlights

- Single phase layered perovskite oxides were synthesized via controlled B-site Fe/Mn ratio.
- Partial Mn doping (x = 0.1) enhanced ORR and HOR activity and reduced ASR under air and hydrogen atmospheres.
- SBFMn (x = 0, 0.1, 0.3 and 0.5) exhibited irreversible conductivity degradation and structural phase transition in hydrogen atmosphere.
- SBFMn 1.8-0.2 maintained stable electrical performance and improved crystallinity during thermal cycling in hydrogen atmosphere.

## 1. Introduction

Solid oxide fuel cells (SOFCs) have been regarded as next-generation eco-friendly energy conversion devices due to their high energy efficiency at high temperatures ranging from 600 to 1000 °C and their ability to utilize various fuels such as hydrogen, natural gas, and carbon monoxide. Typically, the SOFC consists of a cathode, an electrolyte, and an anode, where the oxygen reduction reaction (ORR) occurs at the cathode and the hydrogen oxidation reaction (HOR) occurs at the anode. ORR involves the adsorption of oxygen molecules onto the cathode surface, followed by dissociation into oxygen atoms, reduction to oxygen ions, and the simultaneous formation of oxygen vacancies. HOR refers to the reaction between hydrogen and oxygen ions at the anode, which produces water and releases electrons. The performance of an SOFC is enhanced as the reaction rates of ORR and HOR increase. Because the cathode and anode operate under oxidizing and reducing conditions, different materials have been employed for each electrode to meet the corresponding environmental requirements [1, 2]. However, using different materials for the cathode and anode complicates the manufacturing process and leads to increased high thermal processing costs due to the different sintering temperatures of the applied materials. This factor serves as a significant limitation to the commercialization of SOFCs [2].

To address these issues, symmetrical solid oxide fuel cells (SSOFCs) have been introduced as a potential solution. SSOFCs are designed such that the same electrode material can function as both the cathode and anode in a single cell, which simplifies the manufacturing process and reduces production costs [3]. Furthermore, the use of a single electrode material enables reversible electrochemical reactions, allowing the system to operate not only as an SOFC but also as a solid oxide electrolysis cell (SOEC) [2, 4].

Various transition-metal-based oxides have been suggested as SSOFC electrode materials. In particular, layered perovskite structures have received considerable attention due to their ability to form a higher concentration of oxygen vacancies compared to conventional perovskites, resulting in enhanced catalytic activity for both ORR and HOR. Representative examples include oxide systems such as $PrBaFe_2O_{5+d}$, $SmBaMn_2O_{5+d}$, and $PrBa_{0.8}Ca_{0.2}Mn_2O_{5+d}$ [5-8]. However, many of the reported symmetrical electrode materials still exhibit limitations, including lower electrical conductivity compared to conventional cathode or anode materials, uneven catalytic activity putting either ORR or HOR at a disadvantage and poor structural stability under reducing conditions [9, 10]. To overcome these issues, it is necessary to develop new electrode materials that maintain a stable crystal structure in both oxidizing and reducing atmospheres while simultaneously exhibiting balanced catalytic activity for ORR and HOR [11].

Therefore, in this study, Sm and Ba were applied to the A-site and Fe and Mn to the B-site of the layered perovskite to develop SSOFC electrode materials with enhanced catalytic activity, long-term durability and chemical stability. Specifically, compositions of $SmBa(Fe_{1-x}Mn_x)_2O_{5+d}$ (SBFMn, x = 0, 0.1, 0.3 and 0.5) were synthesized and investigated in terms of their electrical and electrochemical properties to evaluate their suitability as SSOFC electrodes. In addition, crystallographic analysis was performed to investigate the changes in properties with composition. The composition exhibiting the lowest area-specific resistance (ASR) was selected to study phase transitions under high-temperature reducing conditions, and its stability under repeated thermal and electrical conditions was evaluated through electrical conductivity measurements.

## 2. Experimental

### 2.1 Powder preparation

The $SmBa(Fe_{1-x}Mn_x)_2O_{5+d}$ (SBFMn, x = 0, 0.1, 0.3 and 0.5) layered perovskite oxide system was synthesized via a solid-phase synthesis method using $Sm_2O_3$ (Alfa Aesar, 99.9%), $BaCO_3$ (Samchun, 99.0%), $Fe_3O_4$ (Kojundo, 99.0%), and $Mn_3O_4$ (Thermo Scientific, 97.0%) as raw materials. Each powder was precisely weighed and uniformly mixed using an agate mortar and a pestle, with a small amount of ethanol to minimize powder loss and suppress the scattering of fine particles. The mixed powder was dried in an oven at 78 °C for 24 hours. The first calcination step was performed at 1000 °C for 6 hours with a heating rate of 5 °C/min. After calcination, the powder was pulverized using an agate mortar and pestle, followed by ball milling. The solvent used during ball milling, 99% acetone, was evaporated in an oven at 78 °C, and the resulting powder was subjected to a second calcination step at 1300 °C for 8 hours with a heating rate of 5 °C /min to obtain a single phase material. Finally, the heat-treated powder was ground using an agate mortar and pestle, and then sieved through a 100 μm mesh to obtain a homogeneous, fine-grained powder. The prepared powders with the compositions $SmBa(Fe_1Mn_0)_2O_{5+d}$ , $SmBa(Fe_{0.9}Mn_{0.1})_2O_{5+d}$ , $SmBa(Fe_{0.7}Mn_{0.3})_2O_{5+d}$ and $SmBa(Fe_{0.5}Mn_{0.5})_2O_{5+d}$ were named SBFMn 2.0-0.0, SBFMn 1.8-0.2, SBFMn 1.4-0.6, and SBFMn 1.0-1.0 respectively according to their Fe/Mn ratios, which are summarized in Table 1.

### 2.2 X-ray diffraction (XRD)

The crystal structure and phase composition of the synthesized SBFMn powders were analyzed by X-ray diffraction (XRD). For this purpose, a SmartLab XRD instrument

(Rigaku, Japan) equipped with Cu Kα radiation (λ = 1.5418 Å) was used. This equipment was installed at Hanbat National University in 2024 with support from the National University Laboratory Equipment Expansion Project. Measurements were performed at room temperature at analysis conditions of 45 kV and 200 mA. Diffraction patterns were recorded over a 2θ range of 10 ° to 90 °, with a scan speed of 2.5 s/step and a step interval of 0.02 °.

Furthermore, to evaluate the chemical compatibility between the synthesized SBFMn electrode material and the$La_{0.9}Sr_{0.1}Ga_{0.8}Mg_{0.2}O_{3-d}$ (LSGM) electrolyte these powders were mixed at a mass ratio of 1:1. The mixed samples were heat-treated at 1000 °C and 1100 °C for 4 hours, respectively, followed by pulverization and sieving, and XRD analysis was performed under the same conditions as described above. The measured XRD data were analyzed using MDI JADE 6 and SmartLab Studio II programs.

## 2.3 Conductivity measurements

The conductivity measurement samples were prepared by weighing 2.5 g of the synthesized powder, placing it into a metal mold, and pressing it into a rectangular shape under a pressure of $1.5 \times 10^3$ kg/m$^2$. Then, bar type samples with dense microstructure were fabricated by sintering at 1300°C for 3 hours. For the application of the DC 4 probe method, four platinum (Pt) wires were wound around the sample at equal intervals, and the electrical conductivity was measured using a Keithley 2400 source meter in conjunction with a protocol-based system for measuring electrical conductivity developed by our group, details of this procedure can be found in our previously published works [12, 13]. The electrical conductivity was measured in an atmosphere of air, $N_2$ (99.99%), and $H_2$ (3.9%, $H_2$/Ar) by applying a constant current of 0.001 A current while increasing the temperature from 50 ℃ to 900 ℃ in 50 ℃ increments, followed by a decrease from 900 ℃ to 50 ℃ in 50 ℃ in the same steps.

### 2.4 Electrochemical characterization

The samples for electrochemical characterization were prepared as follows. First, $La_{0.9}Sr_{0.1}Ga_{0.8}Mg_{0.2}O_{3-d}$ (LSGM) was used to fabricate the electrolyte support. After weighing 3 g of LSGM powder, the green pellet was pressed in a circular metal mold and sintered at 1400 °C for 6 hours under a pressure of 1.5 x $10^3$ kg/$m^2$ to produce a dense LSGM electrolyte support. The screen-printing ink for the SBFMn electrode was prepared using a solvent and binder system by mixing 5 g of SBFMn powder with 0.1 g of dispersant (KD-1) via ball milling at 160 rpm for 24 hours until a uniform mixture was obtained. A vehicle was prepared by mixing alpha-terpineol (Kanto Chemical) and Butvar (Sigma Aldrich) at a mass ratio of 95:5. Then, 2.17 g of the vehicle was stirred at room temperature to obtain an ink with appropriate viscosity. The ink was screen-printed onto both sides of the LSGM electrolyte support using circular meshes with a diameter of 10 mm, and then heat-treated at 1000 °C for 1 hour to produce the half-cell.

The fabricated half-cell was used to measure the electrochemical impedance characteristics of SBFMn oxide systems using a multichannel impedance analyzer (Ivium-n-Stat, HS Technologies). The resistance was measured in both air and hydrogen atmospheres over the temperature range of 500 °C to 900 °C, with measurements taken at 50 °C intervals.

## 3. Results and discussion

### 3.1 X-ray diffraction (XRD) analysis

XRD analysis was conducted to confirm that the synthesized materials occur as single phases and to analyze their crystal structure according to the Fe/Mn ratio at the B-site. The XRD results are summarized in Figure 1, and characteristic diffraction peaks corresponding to a typical layered perovskite structure, indicative of a single phase, are marked by black bars at the bottom of the pattern. In the $SmBa(Fe_{1-x}Mn_x)_2O_{5+d}$ (SBFMn, x = 0, 0.1, 0.3, and 0.5) oxide system, distinct single phase layered perovskite peaks were observed at 2θ values of 22.6 °, 32.2 °, 39.8 °, 46.3 °, 57.58 °, and 77 °, except for the SBFMn 1.0-1.0 composition. The single phase characterization of these layered perovskites is consistent with several previously reported results from our group [14-16]. In contrast, for the SBFMn 1.0-1.0 composition exhibited low intensity secondary phases, indicating that a small amount of impurities coexisted with the single phase. These secondary phases were identified as $BaMnO_3$ and $SmMnO_3$ [17, 18]. They are considered to have formed either because the reactions among the Sm2O3, BaCO3, and Mn3O4 precursors did not proceed sufficiently during synthesis, or because the excessively high Mn content exceed the compositional stability range in which the layered perovskite structure can exist stably, thereby leading to the formation of secondary phases [19]. In summary, the secondary phases in the SBFMn 1.0-1.0 composition are considered to originate primarily from insufficient precursor reactivity. Secondarily, whenever half of the B-sites or more are occupied by Mn ions, the formation of a pure layered perovskite single-phase becomes difficult.

Figure 1 (b) shows a distinctive shift of the main diffraction peak toward lower angles with increasing Fe content, indicating that the lattice parameter increased accordingly. This behavior is attributed to the difference in the ionic radii of the transition metal ions substituted at the B-site. Although the ionic radii of $Fe^{3+}$ (0.645 Å) and $Mn^{3+}$ (0.645 Å) are identical, the ionic radius of $Fe^{4+}$ (0.585 Å) is larger than that of $Mn^{4+}$ (0.53 Å). Therefore, as the Fe content increases, the average ionic radii at the B-site become larger, resulting in an increase in the lattice constant [20, 21].

The chemical reactivity between the SBFMn electrode material and the $La_{0.9}Sr_{0.1}Ga_{0.8}Mg_{0.2}O_{3-d}$ (LSGM) electrolyte was investigated by mixing the two powders at a 1:1 mass ratio, followed by heat treatment at 1000 °C and 1100 °C, and subsequent XRD analysis. The results are summarized in Figure 2 (a) and (b). Only the diffraction peaks corresponding to the SBFMn electrode and LSGM electrolyte were identified in all samples heat-treated at 1000 °C and 1100 °C. The secondary phase observed near $2\theta = 31.4°$ in the commercial LSGM was identified as belonging to an additive introduced to increase the sintering density of the electrolyte. While this secondary phase remained after heat treatment at 1000 °C, it disappeared at 1100 °C in all compositions except the SBFMn 1.0-1.0 composition. This indicates that the crystal structure of LSGM becomes more stabilized as higher temperatures, resulting in the formation of a complete single phase. The results shown in Figure 2 (a) and (b) confirm that no chemical reaction occurred between the SBFMn electrode materials and the LSGM electrolyte under either heat treatment condition, indicating that the risk of interfacial resistance or mechanical instability during operation under elevated temperatures due to secondary phase formation is negligible. In addition, a sintering temperature of 1000 °C was selected for half cell fabrication in order to preserve the porous electrode microstructure and to ensure sufficient gas diffusion pathways.

### 3.2 Electrochemical performance depending on Fe/Mn ratios

The area specific resistance (ASR) results of $SmBa(Fe_{1-x}Mn_x)_2O_{5+d}$ (SBFMn, x = 0, 0.1, 0.3, and 0.5) electrodes measured in air and 3.9% hydrogen atmospheres are shown in Figure 3 (a) and (b).

As shown in Figure 3 (a), under air atmosphere, the ASR of SBFMn 1.8-0.2, which contains the lowest Mn content, was found to be the lowest for all temperatures above 600 °C, with values of 1.95, 0.45, 0.14, and 0.05 $\Omega\cdot cm^2$ at 600 °C, 700 °C, 800 °C, and 900 °C, respectively. The activation energy was also the lowest for SBFMn 1.8-0.2, calculated to be 1.046 eV. These results suggest that SBFMn 1.8-0.2 exhibits the highest electrocatalytic activity toward the oxygen reduction reaction (ORR). Furthermore, the lower ASR and activation energy observed for SBFMn 1.8-0.2 compared to SBFMn 2.0-0.0 imply that partial substitution of Fe with a small amount of Mn can effectively enhance ORR performance. The low ASR observed in the SBFMn 1.8-0.2 composition is attributed to the fact that a small amount of Mn doping effectively increases the oxygen vacancy concentration and maximizes the redox activity of the Fe-O-Mn bonds, thereby promoting charge transfer. In contrast, excessive Mn doping ($x \geq 0.3$) may hinder the conduction pathways due to lattice distortion and the accumulation of excessive defects, ultimately leading to performance degradation [22]. The ASR results obtained under hydrogen atmosphere are presented in Figure 3 (b). The lowest ASR values were observed for the SBFMn 1.8-0.2 composition at all temperatures except 900 °C. For instance, ASR values of 6.23 $\Omega\cdot cm^2$, 1.27 $\Omega\cdot cm^2$, and 0.44 $\Omega\cdot cm^2$ were recorded at 600 °C, 700 °C, and 800 °C, respectively. At 900 °C, the lowest ASR was observed for SBFMn 1.0-1.0 as 0.25 $\Omega\cdot cm^2$, while SBFMn 1.8-0.2 exhibited a comparable value of 0.28 $\Omega\cdot cm^2$. These results indicate that SBFMn 1.8-0.2 also shows the most favorable electrochemical performance toward the hydrogen oxidation reaction (HOR) under reducing conditions. This is because a small amount of Mn doping ($x = 0.1$) appropriately increases the oxygen vacancy concentration within the electrode, thereby promoting the adsorption and dissociation of $H_2$ while simultaneously activating the electron transfer pathways of the Fe/Mn redox couples. As a result, the SBFMn 1.8-0.2 composition exhibits the lowest ASR under hydrogen atmosphere, as it possesses structural and electronic features that are favorable for the rate-determining steps (RDS) of HOR even under reducing conditions [19].

Further analysis was conducted to identify the RDS of the oxygen reduction reaction (ORR) and hydrogen oxidation reaction (HOR) in the SBFMn 1.8-0.2 composition. The total resistance, measured under both air and hydrogen atmospheres, was deconvoluted into a high-frequency region (HF, $2.5 \times 10^5$ Hz to 1 Hz) and a low-frequency region (1 Hz to 0.05 Hz), which were designated as $R_1$ and $R_2$, respectively. The fitting results for $R_1$ and $R_2$ under air atmosphere and hydrogen atmosphere are presented in Figure 4 (a) and (c) respectively. Visual comparisons of the relative magnitudes of $R_1$ and $R_2$ at various temperatures are shown in Figure 4 (b) and (d).

In air atmosphere, $R_2$ was larger than $R_1$ at temperatures below 550 °C, whereas $R_1$ became the dominant component above 600 °C. $R_1$ corresponds to the high frequency process associated with oxygen ion transfer at the electrode-electrolyte interface, while $R_2$ reflects the low frequency process related to oxygen molecule adsorption on the electrode surface and their diffusion into the electrode interior [23]. As the temperature increased, $R_2$ gradually decreased and the contribution of $R_1$ increased. Above 800 °C, $R_1$ remained the largest resistance component, although the relative contribution of $R_1$ towards the total resistance it exhibited a slight decrease. These results indicate that, in the high temperature region, the rate determining step (RDS) of the ORR is governed by the oxygen ion transfer process represented by $R_1$.

In contrast, the relative contribution of $R_2$, the low frequency resistance which arises from the adsorption of oxygen molecules onto the electrode surface and their diffusion into the electrode interior, was observed to decrease gradually with increasing temperature [15, 24, 25]. This trend was visualized in Figure 4 (a) and (b).

Under hydrogen atmosphere, $R_2$ was more dominant than $R_1$ in the temperature range of 500 °C to 650 °C. This suggests that surface reactions, including hydrogen adsorption and dissociation, govern the rate-determining step (RDS) in this temperature region. In contrast, at temperatures above 700 °C, $R_1$ became dominant over $R_2$, indicating that the charge transfer process at the electrode-electrolyte interface becomes the dominant resistance component in the HOR mechanism [26]. The results are presented in Figure 4 (c) and (d).

Considering the overall results presented in Figure 4, the total polarization resistance decreased with increasing temperature under both air and hydrogen atmospheres. This decrease was accompanied by a reduction in the low frequency component ($R_2$) and an increased contribution of the high frequency component ($R_1$). These trends indicate that, as the temperature increases, electrochemical processes occurring within the electrode bulk and at the electrode-electrolyte interface play a more significant role in determining electrode performance than surface reactions. Consequently, in the high temperature region, the interfacial charge transfer process becomes the dominant RDS.

### 3.3 Electrical conductivity as a function of oxygen partial pressure

The electrical conductivity results of $SmBa(Fe_{1-x}Mn_x)_2O_{5+d}$ (SBFMn, x = 0, 0.1, 0.3, and 0.5) measured in air, nitrogen, and 3.9 % hydrogen atmospheres are summarized in Figure 5.

In Figure 5 (a) and (b), which represent the conductivity characteristics under air and nitrogen atmospheres, respectively, a transition from metal-insulator transition (MIT)-like behavior to semiconductor behavior was observed as the Mn content increased. For example, the SBFMn 1.8-0.2 composition exhibited a conductivity of 0.105 S/cm at 50 °C, which increased to a maximum of 5.85 S/cm at 650 °C, followed by a decrease to 4.08 S/cm at 900 °C. In contrast, the SBFMn 1.0-1.0 composition, with a higher Mn content, exhibited significantly lower conductivity values, increasing from approximately 0.0008 S/cm at 50 °C to 0.88 S/cm at 600 °C and 1.33 S/cm at 900 °C. Under air atmosphere, no significant difference in electrical conductivity was observed between the heating and cooling processes, whereas under nitrogen atmosphere, a slight decrease in conductivity was observed during cooling compared to heating. In addition, the higher electrical conductivity measured under the air atmosphere compared to that under the nitrogen atmosphere indicates that the SBFMn electrode material exhibits p-type conduction, where holes are the dominant charge carriers. This is consistent with the typical behavior of p-type conductors, in which conductivity increases under high oxygen partial pressure due to an increase in hole concentration [27, 28].

In addition to the comparison of conduction mechanisms, when the electrical conductivity values at 700 °C under air atmosphere are compared, the SBFMn 2.0-0.0 composition exhibited the highest conductivity at 10.73 S/cm. The other compositions (SBFMn 1.8-0.2, SBFMn 1.4-0.6, and SBFMn 1.0-1.0) showed conductivity values of 5.09 S/cm, 4.17 S/cm, and 0.87 S/cm, respectively, indicating a decreasing trend in conductivity with increasing Mn content. A similar trend was also observed under nitrogen atmosphere, as shown in Figure 5 (b), where the SBFMn 2.0-0.0 composition again exhibited the highest conductivity of 2.35 S/cm, followed by 1.46 S/cm for SBFMn 1.8-0.2, 1.33 S/cm for SBFMn 1.4-0.6, and 0.73 S/cm for SBFMn 1.0-1.0. In both atmospheres, a consistent trend of decreasing electrical conductivity with increasing Mn content was observed.

This behavior is attributed to the lower metal-oxygen (M-O) orbital overlap in Mn-O bonds compared to Fe-O bonds, as well as the smaller ionic radius of Mn ions relative to Fe ions. Upon increase in Mn doping, the reduction in bond angle within the lattice induces the formation of lattice defects and deteriorates the connectivity of the M-O-M conduction pathway. As a result, the mobility of charge carriers (i.e., electron holes) is hindered, leading to a decrease in electrical conductivity [29-31]. In addition to the reduced mobility, an increase in Mn content also decreases the concentration of charge carriers. In perovskite type ferrites, electron hole carriers are mainly associated with the $Fe^{4+}$ species, while Mn exists predominantly as $Mn^{4+}$ under the oxygen partial pressure used in this study and contributes only minimally to the formation of electron holes providing p-type transport [32]. Furthermore, doping with $Mn^{4+}$ reduces the amount of $Fe^{4+}$ via the charge compensation mechanism. Consequently, increasing the Mn content results in a decrease in hole concentration, further contributing to the reduction in electrical conductivity. Thus, the Mn content plays a critical role in determining the electrical conductivity of SBFMn, and precise control of the Mn/Fe ratio is essential for optimizing charge transport while maintaining the structural characteristics required for SOFC electrode applications.

As shown in Figure 5 (c), which presents the electrical conductivity measured under hydrogen atmosphere, the SBFMn 1.8-0.2 composition exhibited the highest conductivity of 2.59 S/cm at 700 °C. The conductivities of SBFMn 2.0-0.0, SBFMn 1.4-0.6, and SBFMn 1.0-1.0 were measured as 1.11 S/cm, 1.21 S/cm, and 0.14 S/cm, respectively. These results suggest that a small amount of Mn enhances electrical conductivity under hydrogen atmosphere, indicating that optimal charge transport can be achieved at a specific composition. In contrast, when the Mn content exceeded that of the SBFMn 1.8-0.2 composition, the difference in ionic radii between B-site cations induces lattice contraction, leading to structural distortion.

In addition, semiconducting behavior was observed in the temperature range of 50 ℃ to 350 ℃ of the heating cycle, followed by a sharp decline in electrical conductivity between 400 ℃ and 500 ℃, and then a subsequent steep increase with further temperature rise. For example, in the SBFMn 1.8-0.2 composition, the electrical conductivity increased to 8.11 S/cm up to 350 ℃, then dropped sharply to 0.003 S/cm at 450 ℃, and subsequently increased again to 2.77 S/cm at 900 ℃. During the cooling process, typical semiconductor behavior was again observed across the whole temperature range. SBFMn 1.8-0.2 serves only as an example, the very same behavior can be observed in all SBFMn compositions studied. This variation in conductivity is attributed to structural transformations occurring under reducing conditions, as confirmed by the XRD analysis shown in Figure 6 (a). In this analysis, samples were exposed to a hydrogen atmosphere for 1 hour at 20 °C, 450 °C, and 900 °C, followed by XRD characterization at room temperature.

To investigate the crystallographic characteristics in detail, structural analysis and lattice parameter calculations were performed using the Jade 6 program. Samples exposed to hydrogen atmosphere at 25 °C and 450 °C exhibited a cubic structure, with a slight increase in lattice constants with rising temperature: 3.921 Å at 25 °C and 3.9232 Å at 450 °C. The sample treated at 900 °C exhibited a structural transition to an orthorhombic structure, with lattice parameters calculated as a = 3.959 Å, b = 3.9638 Å, and c = 7.6748 Å.

This lattice expansion of the cubic structure between 25 °C and 450 °C is attributed to the generation of oxygen vacancies at rising temperatures under reducing conditions in addition to the increased thermal vibrations at elevated temperatures [33]. The transition from cubic to orthorhombic structure comes with a reduction in crystal symmetry. The significant drop in electrical conductivity observed near 450 °C is considered to be the result of this phase transition rather than from material decomposition, as supported by the structural change shown in Figure 6 (a). Further increase of temperature after this structure transition leads to a redistribution of oxygen vacancies. Through this structural rearrangement, the migration pathways for charge carriers were re-established, which appears to have contributed to the recovery of electrical conductivity with increasing temperatures from 600 °C to 900 °C.

In addition to these structural factors the nonlinear conductivity behavior observed under the initial heating under hydrogen atmosphere in Figure 5 (c) can be attributed to the oxidation state of manganese. In the low-temperature region around 450 °C of the reducing atmosphere, $Mn^{4+}$ exists as the dominant oxidation state, Mn has not been sufficiently reduced at these low temperatures and a high $Mn^{4+}$ fraction remains. With increasing temperature, a complex distribution of oxidation state emerges, in which $Mn^{2+}$, $Mn^{3+}$, and $Mn^{4+}$ coexist [34]. Generally a $Mn^{4+}$ dominance leads to a decrease in both the concentration and mobility of charge carriers. Mixed valence states on the other hand promote hole transport via the small polaron hopping mechanism, thereby enhancing electronic conductivity [35].

As shown in Figure 5 (c), the electrical conductivity behavior under hydrogen atmosphere exhibited a distinct difference between heating and cooling, unlike the trends observed under air and nitrogen atmospheres. During heating, complex conductivity behavior was observed, which is mainly attributed to structural transformations, whereas during cooling, all compositions exhibited consistent semiconductor behavior. This suggests that no further structural change occurred during the cooling process, indicating that the structural transitions induced during heating under hydrogen atmosphere are irreversible.

To demonstrate that the observed structural transformations are unique to hydrogen atmospheres, additional structural analysis was performed using in situ XRD measurements in an air atmosphere at increasing temperatures of 25 °C, 450 °C, and 900 °C. The results are summarized in Figure 6 (b). At 25 °C, 450 °C, and 900 °C under air atmosphere, a cubic structure was consistently retained, and the lattice parameters were found to increase slightly to 3.9194 Å, 3.9398 Å, and 3.9682 Å, respectively. As previously discussed, the increase in lattice parameter with temperature arises not only from enhanced thermal vibrations but also from a slight loss of lattice oxygen at elevated temperatures, which shifts the Fe valence from $Fe^{4+}$ toward $Fe^{3+}$. The increased fraction of $Fe^{3+}$ with its larger ionic radius compared to $Fe^{4+}$ further contributes to the observed lattice expansion. Although the lattice parameter increased with temperature, no phase transition was observed, in contrast to the behavior under hydrogen atmosphere. This confirms that the structural transformation is a phenomenon specific to the reducing environment.

To further confirm the long-term stability of electrical conductivity in hydrogen atmosphere, electrical conductivity measurements were performed for 8 cycles for SBFMn 1.8-0.2, which exhibited the highest electrical conductivity. The results are shown in Figure 7. From cycle 2 to cycle 8, the electrical conductivity did not exhibit the nonlinear conductivity behavior displayed through the first heating cycle, neither the sharp drop at 450 °C nor the steep recovery between 700 °C and 900 °C. This confirms the irreversible nature of the phase change from cubic to orthorhombic mentioned above. The strictly linear semiconductor behavior of the conductivity during both heating and cooling cycles 2 to 8 also seems to suggest a stability of Mn oxidation state, the mixed valence state of coexisting $Mn^{2+}$, $Mn^{3+}$, and $Mn^{4+}$, originally achieved by the reduction of dominant $Mn^{4+}$ during the first heating cycle is stable from cycle 2 on.

Figure 7 shows a slight increasing trend in conductivities with repeated measurements from cycle 2 to cycle 8. In addition, XRD analysis was conducted to confirm the structural changes in the sample after 8 electrical conductivity measurement cycle under hydrogen atmosphere, and the results are shown in Figure 6 (a). Compared to the sample heat-treated at 900 °C for 1 h in a hydrogen, the post cycling sample exhibited increased XRD peak intensity and reduced full width at half maximum (FWHM). These changes in the diffraction pattern indicate improved crystallinity and suggest that the crystal structure became progressively more ordered and stabilized during long-term exposure and repeated thermal cycling under reducing conditions, which would explain the slightly better performance during later cycles. Based on these observations, it can be concluded that the SBFMn 1.8-0.2 composition maintains both structural and electrical stability during prolonged operation and repeated thermal cycling in hydrogen atmosphere.

## 4. Conclusion

In this study, the structural stability, electrochemical performance, and electrical conductivity behavior of $SmBa(Fe_{1-x}Mn_x)_2O_{5+d}$ (x=0, 0.1, 0.3, and 0.5) layered perovskite oxide systems were systematically investigated under various oxygen partial pressure conditions.

According to XRD analysis, a stable single phase layered perovskite structure was formed for all compositions except for SBFMn 1.0-1.0, and chemical compatibility with the LSGM electrolyte was confirmed after heat treatment, with no secondary phase formation observed.

Electrochemical characterization revealed that the SBFMn 1.8-0.2 composition, containing a small amount of Mn, exhibited the lowest ASR and activation energy in both air and hydrogen atmospheres, and demonstrated the highest electrochemical performance in both ORR and HOR.

Electrical conductivity measurements showed that conductivity generally decreased with increasing Mn content under air and nitrogen atmospheres due to a reduced orbital overlap in the B-O-B bonding and a decrease in hole concentration. However, under hydrogen atmosphere, a small amount of Mn incorporation enhanced the electrical conductivity, suggesting that the Fe/Mn ratio plays an important role in determining charge transport behavior under reducing conditions. XRD confirmed that an irreversible cubic to orthorhombic phase transition occurred only under hydrogen atmosphere, correlating with the sharp conductivity drop observed during the first heating cycle. In addition, repeated conductivity measurements over 8 thermal cycles in hydrogen atmosphere for the SBFMn 1.8-0.2 composition revealed a slight increase in electrical conductivity, with no recurrence of the sharp conductivity drop at 450 °C observed during the initial cycle.

XRD analysis of the cycled sample showed increased diffraction peak intensity and reduced FWHM, indicating that the crystal structure became increasingly ordered and stabilized after prolonged hydrogen exposure and repeated thermal cycling.

Overall, the effects of Mn doping on the structural and functional properties were identified, and it was demonstrated that a small degree of Mn incorporation can enhance both electrical conductivity and structural stability under reducing conditions. These findings provide valuable insight for future composition design and optimization of SSOFC electrode materials.

## Funding

This work was supported by the Korea government (KETEP) (No. RS-2024-00394769), the Ministry of Education (NRF) (No. RS-2024-00464727), and the Hanbat National University Financial Accounting Research Fund in 2024.

## Acknowledgements

This work was supported by the Human Resources Development of a Korea Institute of Energy Technology Evaluation and Planning (KETEP) grant funded by the Korea government (No. RS-2024-00394769), by the Basic Science Research Program through the National Research Foundation of Korea (NRF) funded by the Ministry of Education (No. RS-2024-00464727), and by the Hanbat National University Financial Accounting Research Fund in 2024.

## Declarations of competing interest

The authors declare that they have no known competing financial interests or personal relationships that could have appeared to influence the work reported in this paper.

## References

[1] S.K. Dwivedi, M. Vishwakarma, Hydrogen embrittlement in different materials: A review, Int. J. Hydrogen Energy 45 (2020) 23988–24013. https://doi.org/10.1016/j.ijhydene.2018.09.201

[2] J. C. Ruiz-Morales, J. Canales-Vázquez, J. Peña-Martínez, D. Marrero-López, P. Núñez, On the simultaneous use of $La_{0.75}Sr_{0.25}Cr_{0.5}Mn_{0.5}O_{3-\delta}$ as both anode and cathode material with improved microstructure in solid oxide fuel cells, Electrochim. Acta 52 (2006) 278–284. https://doi.org/10.1016/j.electacta.2006.05.006

[3] J. C. Ruiz-Morales, D. Marrero-López, J. Canales-Vázquez, J. T. S. Irvine, Symmetric and reversible solid oxide fuel cells, RSC Adv. 1 (2011) 1403–1414. https://doi.org/10.1039/C1RA00284H

[4] S. Akkurt, C. Sındırac, T. Özmen Egesoy, E. Ergen, A review on new cobalt-free cathode materials for reversible solid oxide fuel cells, J. Met. Mater. Miner. 33 (2023) 1654–1654. https://doi.org/10.55713/jmmm.v33i3.1654

[5] Y. Gu, Y. Zhang, Y. Zheng, H. Chen, L. Ge, L. Guo, $PrBaMn_2O_{5+\delta}$ with praseodymium oxide nano-catalyst as electrode for symmetrical solid oxide fuel cells, Appl. Catal. B 257 (2019) 117868. https://doi.org/10.1016/j.apcatb.2019.117868

[6] Y. Zhang, H. Zhao, Z. Du, K. Świerczek, Y. Li, High-Performance $SmBaMn_2O_{5+\delta}$ Electrode for Symmetrical Solid Oxide Fuel Cell, Chem. Mater. 31 (2019) 3784–3793. http://dx.doi.org/10.1021/acs.chemmater.9b01012

[7] S.-H. Choi, S. Sengodan, S. Park, Y.-W. Ju, J. Kim, J. Hyodo, H.-Y. Jeong, T. Ishihara, J. Shin, G. Kim, A robust symmetrical electrode with layered perovskite structure for

direct hydrocarbon solid oxide fuel cells: $PrBa_{0.8}Ca_{0.2}Mn_2O_{5+\delta}$, J. Mater. Chem. A 4 (2016) 1747–1753. https://doi.org/10.1039/C5TA08878J

[8] K. Zhu, B. Luo, Z. Liu, X. Wen, Recent advances and prospects of symmetrical solid oxide fuel cells, Ceram. Int. 48 (2022) 8972–8986. https://doi.org/10.1016/j.ceramint.2022.01.258

[9] J. Zamudio-García, L. Caizán-Juanarena, J. M. Porras-Vázquez, E. R. Losilla, D. Marrero-López, A review on recent advances and trends in symmetrical electrodes for solid oxide cells, J. Power Sources 520 (2022) 230852. https://doi.org/10.1016/j.jpowsour.2021.230852

[10] S.P.S. Shaikh, A. Muchtar, M.R. Somalu, A review on the selection of anode materials for solid-oxide fuel cells, Renew. Sustain. Energy Rev. 51 (2015) 1–8. https://doi.org/10.1016/j.rser.2015.05.069

[11] Y. Hou, L. Wang, L. Bian, Y. Wang, K.C. Chou, Excellent Electrochemical Performance of La0.3Sr0.7Fe0.9Ti0.1O3-δ as a Symmetric Electrode for Solid Oxide Cells, ACS Appl. Mater. Interfaces 13 (2021) 22381–22390. https://doi.org/10.1021/acsami.1c02856

[12] K.E. Song, J.W. Lee, Y.R. Lim, S.W. Baek, T.H. Shin, S.K. Lee, H. Schlegl, J.H. Kim, Influence of microstructure and applied current on the electrical conductivity of $SmBaCo_2O_{5+d}$ Cathode in solid oxide fuel cell, Int. J. Hydrogen Energy 47 (2022) 15875–15886. https://doi.org/10.1016/j.ijhydene.2022.03.056

[13] J. M. Im, K. E. Song, H. Schlegl, H. Kang, W. Choi, S.-W. Baek, J.-Y. Park, H.-S. Kim, J. H. Kim, Generation of nanoflowers and nanoneedles on Co-based layered

perovskite of IT-SOFC cathode affecting electrical conductivities, Int. J. Hydrogen Energy 48 (2023) 35229–35239. https://doi.org/10.1016/j.ijhydene.2023.05.327

[14] K. E. Song, H. Schlegl, H. Kang, W. Choi, J. H. Kim, Electrochemical characteristic of non-stoichiometric $SmBa_{0.45}Sr_{0.5}Co_2O_{5+d}$ layered perovskite oxide system for IT-SOFC cathode, Int. J. Hydrogen Energy 48 (2023), 17664–17676. https://doi.org/10.1016/j.ijhydene.2023.01.255

[15] J. M. Im, H. Schlegl, J.-Y. Park, S.-W. Baek, J. H. Kim, Electrochemical properties of B-site non-stoichiometric layered perovskite $SmBa_{0.5}Sr_{0.5}Co_xO_{5+d}$ (x=1.9-2.1) cathodes for IT-SOFC, Ceram. Int. 50(2024) 24565–24575. https://doi.org/10.1016/j.ceramint.2024.04.192

[16] K. S. Baek, S.-W. Baek, H. Kang, W. Choi, J.-Y. Park, S. Stefan, S. K. Lee, J. H. Kim, Electrical conductivity characteristics of Sr substituted layered perovskite cathode ($SmBa_{0.5}Sr_{0.5}Co_2O_{5+d}$) for intermediate temperature-operating solid oxide fuel cell, Ceram. Int. 48 (2022) 15770–15779. https://doi.org/10.1016/j.ceramint.2022.02.114

[17] S. Singh, S. Maiti, S. Rani, H. Raj, R.S. Bisht, S.K. Panigrahi, I. Tyagi, "Ti doped $BaMnO_3$ perovskite structure as photocatalytic agent for the degradation of noxious air and water pollutants," SN Applied Sciences 2 (2020) 310. https://doi.org/10.1007/s42452-020-2121-9

[18] J. Mantilla, M. Morales, W. Venceslau, L. Corredor, P.C. Morais, F.F.H. Aragon, S.W. da Silva, J.A. Coaquira, "Field-driven spin reorientation in $SmMnO_3$ polycrystalline powders," Journal of Alloys and Compounds 845 (2020) 156327. https://doi.org/10.1016/j.jallcom.2020.156327

[19] D. Han, Z. Song, B. Liu, X. Zhang, J. Liu, Y. Huang, C. Xing, J. Zhang, “Mn doping induces oxygen-rich vacancies to regulate $Co^{2+}$ cyclic regeneration and synergistically promote PMS activation and pollutant degradation,” Journal of Molecular Structure, vol. 1349, 2026, 143895. https://doi.org/10.1016/j.molstruc.2025.143895

[20] M. Gaudon, C. Laberty-Robert, F. Ansart, P. Stevens, A. Rousset, Preparation and characterization of $La_{1-x}Sr_xMnO_{3+\delta}$ ($0 \leq x \leq 0.6$) powder by sol-gel processing, Solid State Sci. 4 (2002) 125–133. https://doi.org/10.1016/S1293-2558(01)01208-0

[21] T. Nakamura, G. Petzow, L. J. Gauckler, Stability of the perovskite phase $LaBO_3$ (B = V, Cr, Mn, Fe, Co, Ni) in reducing atmosphere I. Experimental results, Mater. Res. Bull. 14 (1979) 649–659. https://doi.org/10.1016/0025-5408(79)90048-5

[22] S. Wang, P. Han, Y. Zhao, W. Sun, R. Wang, X. Jiang, C. Wu, C. Sun, H. Wei, “Oxygen-vacancy-mediated $LaFe_{1-x}Mn_xO_{3-}\delta$ perovskite nanocatalysts for degradation of organic pollutants through enhanced surface ozone adsorption and metal doping effects,” Nanoscale 13 (2021) 12874–12884. https://doi.org/10.1039/d1nr03055h

[23] J. Liu, F. Jin, X. Yang, B. Niu, Y. Li, T. He, $YBaCo_2O_{5+}\delta$-based double-perovskite cathodes for intermediate-temperature solid oxide fuel cells with simultaneously improved structural stability and thermal expansion properties, Electrochimica Acta, 297 (2019) 344–354. https://doi.org/10.1016/j.electacta.2018.11.214

[24] J. H. Kim, J. T. S. Irvine, Characterization of layered perovskite oxides $NdBa_{1-x}Sr_xCo_2O_{5+\delta}$ (x=0 and 0.5) as cathode materials for IT-SOFC, Int. J. Hydrogen Energy 37 (2012) 5920–5929. https://doi.org/10.1016/j.ijhydene.2011.12.150

[25] J.-H. Kim, A. Manthiram, Layered $LnBaCo_2O_{5+\delta}$ perovskite cathodes for solide oxide fuel cells: an overview and perspective, J. Mater. Chem. A 3 (2015) 24195–24210. https://doi.org/10.1039/C5TA06212H

[26] J. Yan, H. Chen, Y. W. Li, S.-D. Li, Z. Shao, Bifunctional electrocatalysts $Pr_{0.5}Sr_{0.5}Cr_{0.1}Fe_{0.9-x}Ni_xO_{3-\delta}$ (x = 0.1, 0.2) for the HOR and ORR of a symmetric solid oxide fuel cell, J. Mater. Chem. A 11(2023) 21839–21845. https://doi.org/10.1039/D3TA03475E

[27] S. Kim, Y. L. Yang, R. Christoffersen, A. J. Jacobson, Oxygen permeation, electrical conductivity and stability of the perovskite oxide $La_{0.2}Sr_{0.8}Cu_{0.4}Co_{0.6}O_{3-x}$, Solid State Ionics 104 (1997) 57–65. https://doi.org/10.1016/S0167-2738(97)00427-X

[28] K. E. Song, H. Schlegl, C. G. Kim, K. S. Baek, Y. R. Lim, J. H. Nam, H. S. Kim, J. H. Kim, Electrical conductivity properties of porous $SmBaCo_2O_{5+d}$ layered perovskite oxide systems for solid oxide fuel cell, Ceram. Int. 48 (2022) 28649–28658. https://doi.org/10.1016/j.ceramint.2022.06.179

[29] K. T. Lee, A. Manthiram, Effect of cation doping on the physical properties and electrochemical performance of $Nd_{0.6}Sr_{0.4}Co_{0.8}M_{0.2}O_{3-\delta}$ (M = Ti, Cr, Mn, Fe, Co, and Cu) cathodes, Solid State Ionics 178 (2007) 995–1000. https://doi.org/10.1016/j.ssi.2007.04.010

[30] R. Song, D. Guo, A. Li, Y. W. Liu, Z. Jin, C. Lu, D. Qiu, B. Niu, B. Wang, Sr and Mn co-doping PrBaFe2O5+δ optimizes the electrochemical performance and stability of solid oxide fuel cell cathode, J. Alloys Compd. 1005 (2024) 176231. https://doi.org/10.1016/j.jallcom.2024.176231

[31] Y.-P. Fu, C.-H. Li, J. Ouyang, S.-H. Hu, K.-W. Tay, Definition of a State-of-Energy Indicator (SoE) for Electrochemical Storange Devices: Application for Energetic Availability Forecasting, J. Electrochem. Soc. 159 (2012) 426–435. https://doi.org/10.1149/2.075208jes

[32] G. Raimondi, R. Merkle, A. Longo, F. Giannici, O. Mathon, C. J. Sahle, J. Maier, Interplay of chemical, electronic, and structural effects in the triple-conducting $BaFeO_3$–$Ba(Zr,Y)O_3$ solid solution, Chemistry of Materials, 35 (2023) 8945–8957. https://doi.org/10.1021/acs.chemmater.3c01538

[33] A. A. Markov, K. Y. Chesnokov, M. V. Patrakeev, I. A. Leonidov, A. V. Chukin, O. N. Leonidova, V. L. Kozhevnikov, Oxygen non-stoichiometry and mixed conductivity of $La_{0.5}Sr_{0.5}Fe_{1-x}Mn_xO_{3-\delta}$, J. Solid State Electrochem. 20 (2016) 225–234. https://doi.org/10.1007/s10008-015-3027-0

[34] S. S. Nikitin, A. D. Koryakov, E. A. Antipinskaya, A. A. Markov, M. V. Patrakeev, The effect of temperature and oxygen partial pressure on the concentration of iron and manganese ions in $La_{1/3}Sr_{2/3}Fe_{1-x}Mn_xO_{3-\delta}$, Phys. Chem. Chem. Phys. 26 (2024) 1125–1134. https://doi.org/10.1039/d3cp05421g

[35] R. B. Wexler, G. S. Gautam, E. B. Stechel, E. A. Carter, Factors Governing Oxygen Vacancy Formation in Oxide Perovskites, J. Am. Chem. Soc. 143 (2021) 13212–13227. https://doi.org/10.1021/jacs.1c05570

## Figure captions

Figure 1. (a) X-ray diffraction (XRD) patterns of SBFMn oxide systems and (b) enlarged view of the main peak region between 31 ° and 33 °

Figure 2. XRD results of LSGM-SBFMn composites heat treated at (a) 1000 ℃ and (b) 1100 ℃

Figure 3. Comparison of the area specific resistance of SBFMn : (a) in air and (b) in hydrogen atmosphere

Figure 4. Impedance characteristics and resistance behavior of SBFMn 1.8-0.2 composition at different temperatures. (a) Impedance plots measured in air, (b) Temperature dependence of $R_1$ and $R_2$ components in air, (c) Impedance plots measured in hydrogen atmosphere, (d) Temperature dependence of $R_1$ and $R_2$ components in hydrogen atmosphere

Figure 5. Electrical conductivity of SBFMn measured under (a) air, (b) nitrogen, and (c) hydrogen atmospheres

Figure 6. XRD patterns of SBFMn 1.8-0.2 samples : after heat treatment at 25 ℃, 450 ℃, and 900 ℃ (a) in hydrogen atmosphere and ex-situ measurement, and measured (b) in situ under air atmosphere at corresponding temperature

Figure 7. Electrical conductivity of SBFMn 1.8-0.2 under hydrogen atmosphere over 8 thermal cycles

## Table captions

Table 1. Sample abbreviation

Table 2. ASR of SBFMn 1.8–0.2 electrode in air and hydrogen atmospheres

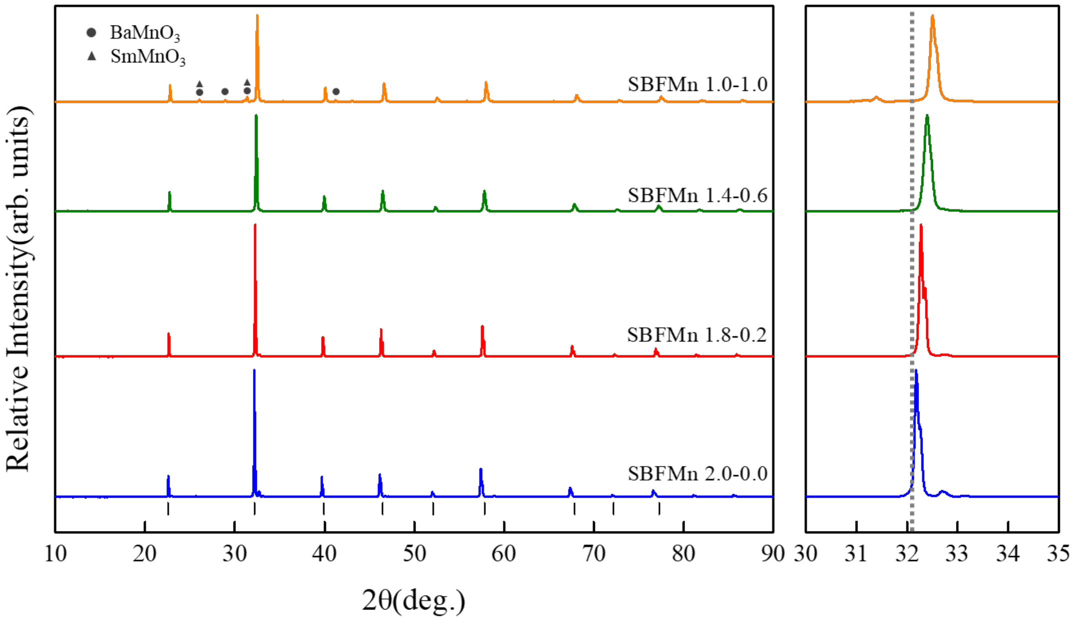

(a) (b)

Fig 1. (a) X-ray diffraction (XRD) patterns of SBFMn oxide systems and (b) enlarged view of the main peak region between 31 ° and 33 °

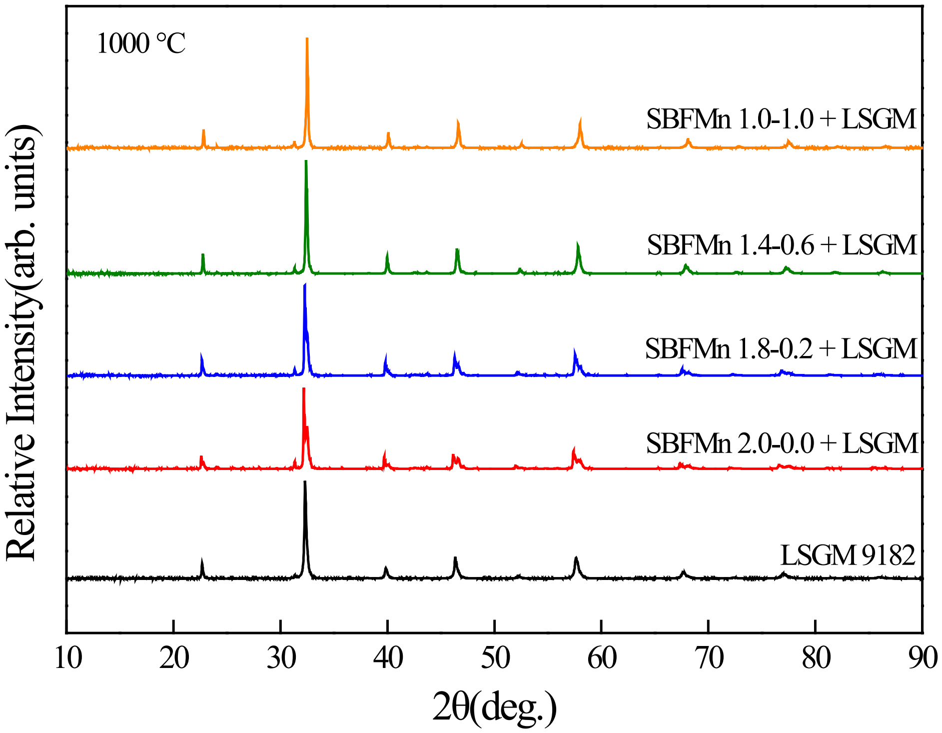
1000 °C
SBFMn 1.0-1.0 + LSGM
SBFMn 1.4-0.6 + LSGM
SBFMn 1.8-0.2 + LSGM
SBFMn 2.0-0.0 + LSGM
LSGM 9182
Relative Intensity(arb. units)
10
20
30
40
50
60
70
80
90
2θ(deg.)

(a)

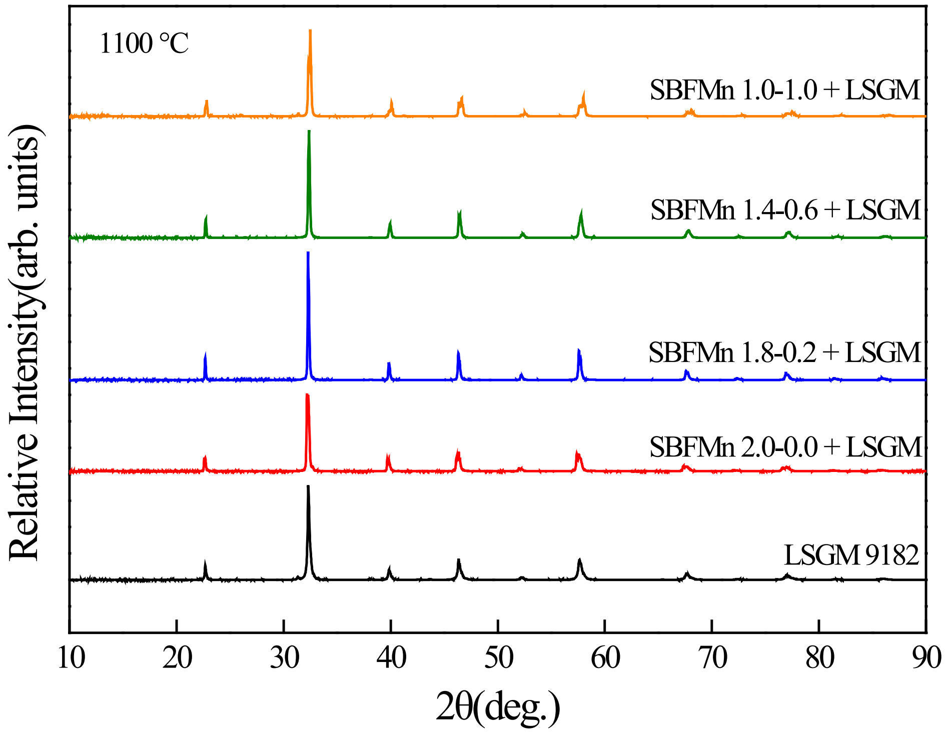

(b)

Fig 2. XRD results of LSGM-SBFMn composites heat treated at (a) 1000 °C and (b) 1100 °C

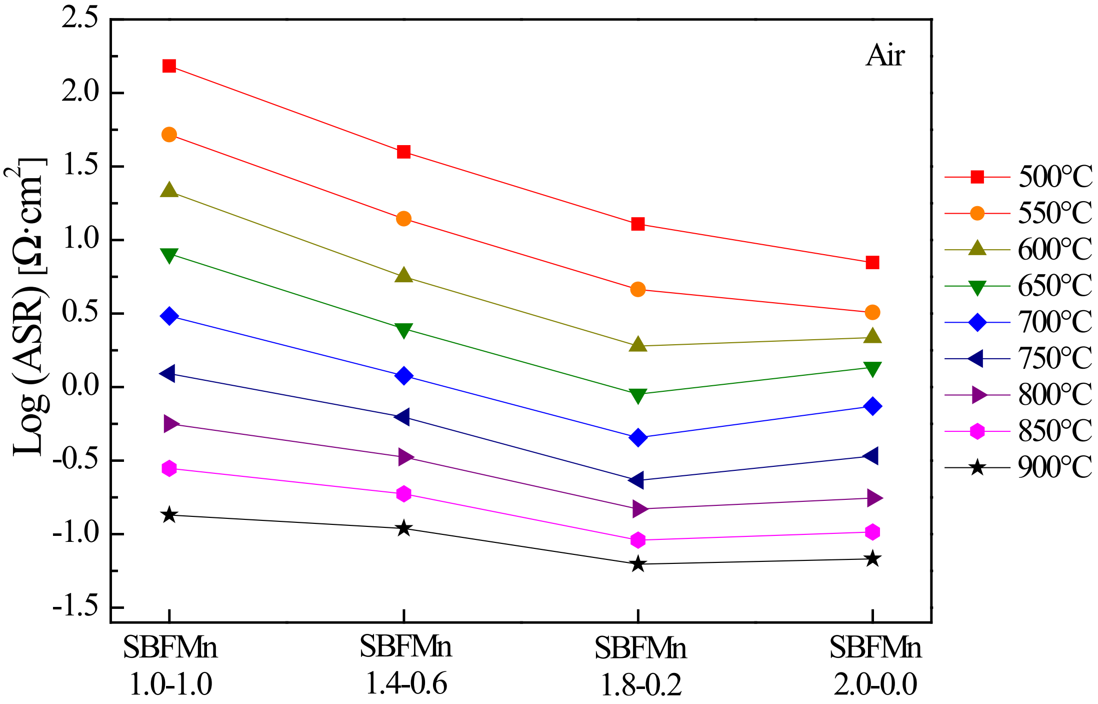

Air
Log (ASR) [Ω·cm$^2$]
2.5
2.0
1.5
1.0
0.5
0.0
-0.5
-1.0
-1.5
SBFMn 1.0-1.0
SBFMn 1.4-0.6
SBFMn 1.8-0.2
SBFMn 2.0-0.0
500°C
550°C
600°C
650°C
700°C
750°C
800°C
850°C
900°C

(a)

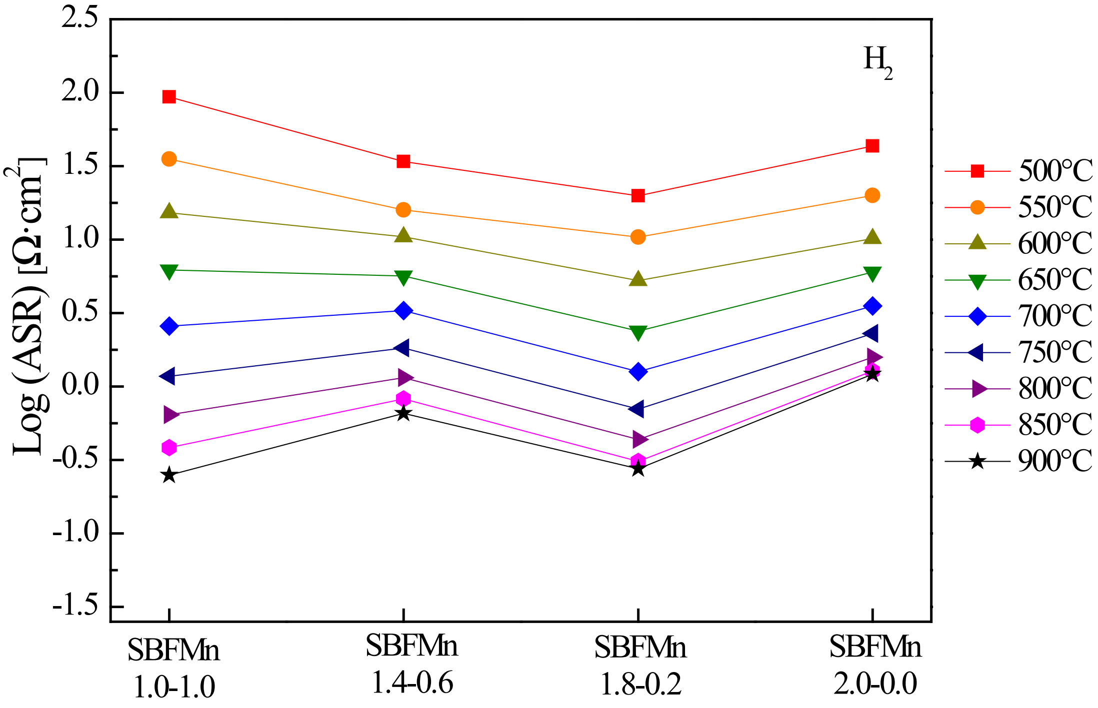

(b)

Fig 3. Comparison of the area specific resistance of SBFMn : (a) in air and (b) in hydrogen atmosphere

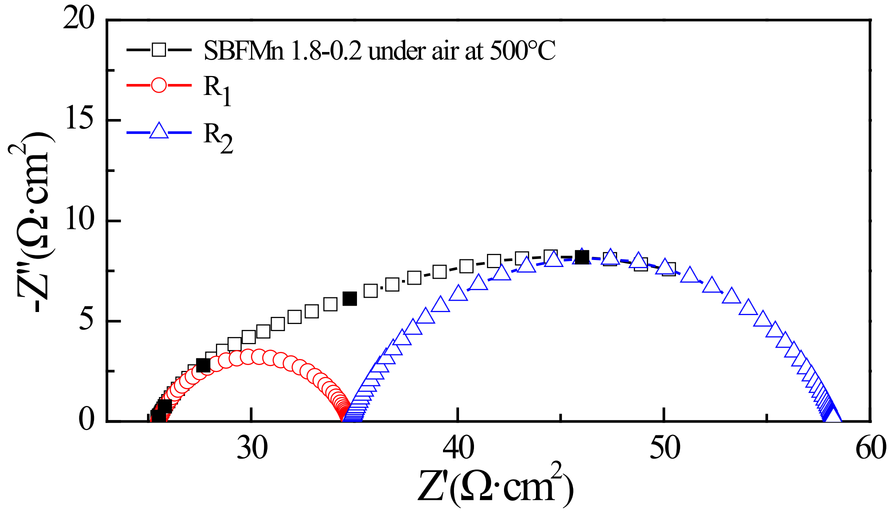
SBFMn 1.8-0.2 under air at 500°C
R1
R2
-Z''(Ω·cm2)
Z'(Ω·cm2)
0
5
10
15
20
30
40
50
60

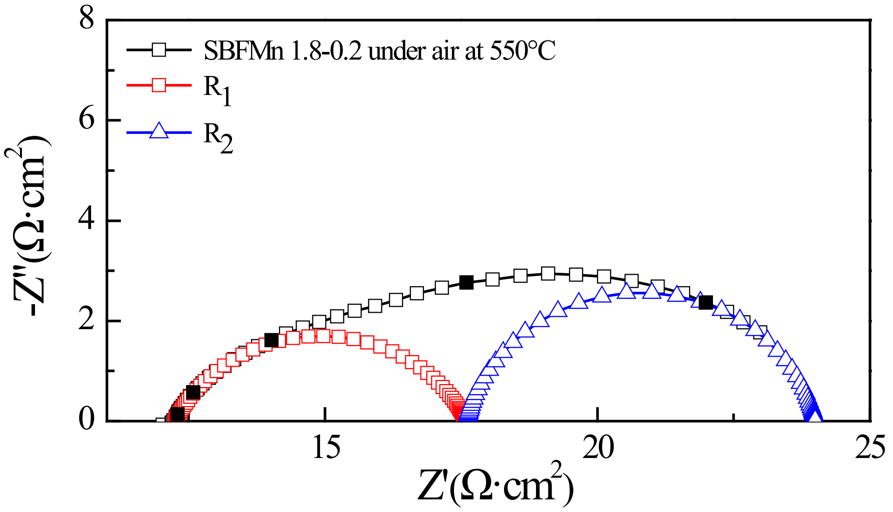
SBFMn 1.8-0.2 under air at 550°C
R1
R2
-Z''(Ω·cm2)
Z'(Ω·cm2)
0
2
4
6
8
15
20
25

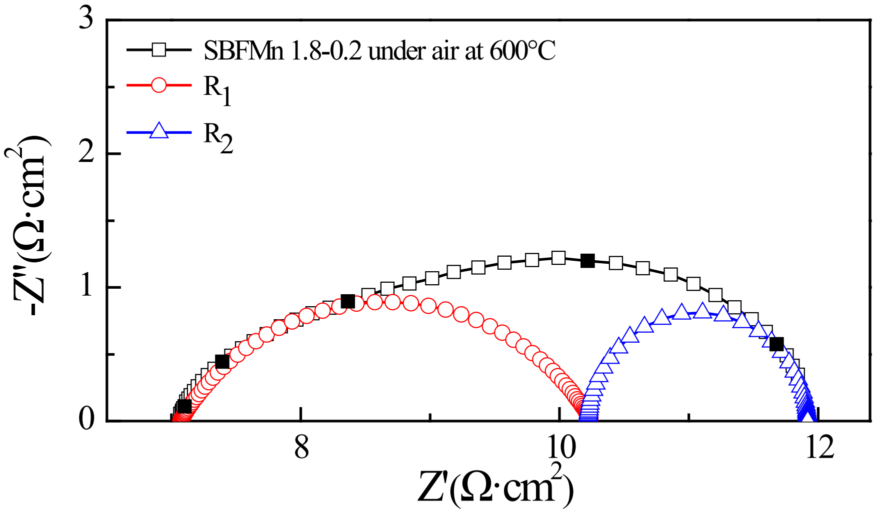
SBFMn 1.8-0.2 under air at 600°C
R1
R2
-Z''(Ω·cm2)
Z'(Ω·cm2)
0
1
2
3
8
10
12

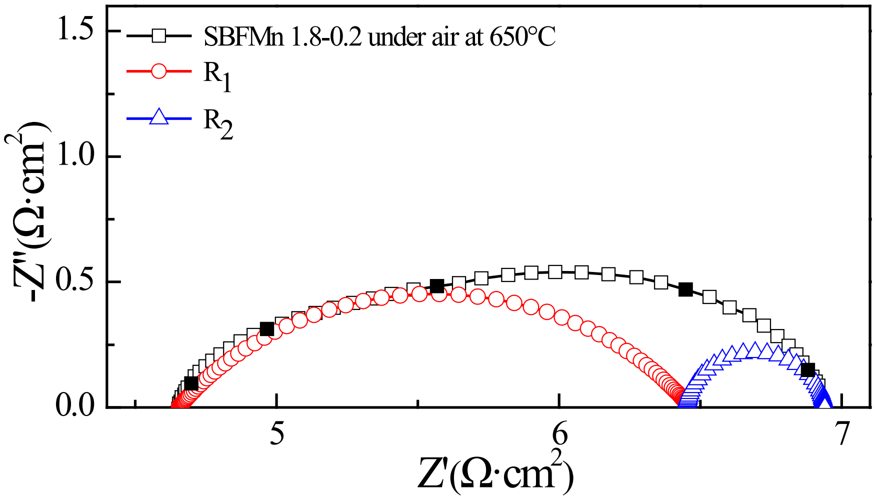
SBFMn 1.8-0.2 under air at 650°C
R1
R2
-Z''(Ω·cm2)
1.5
1.0
0.5
0.0
5
6
7
Z'(Ω·cm2)

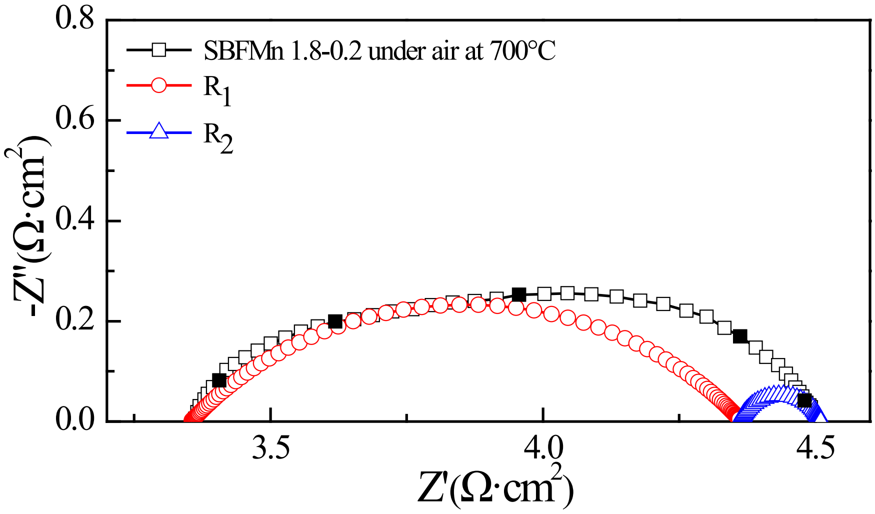
SBFMn 1.8-0.2 under air at 700°C
R1
R2
-Z''(Ω·cm2)
0.8
0.6
0.4
0.2
0.0
3.5
4.0
4.5
Z'(Ω·cm2)

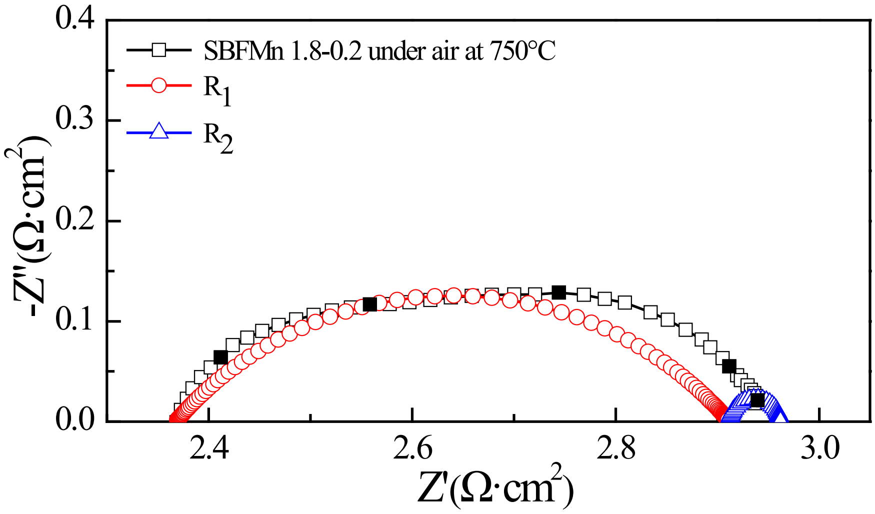
SBFMn 1.8-0.2 under air at 750°C
R1
R2
-Z''(Ω·cm2)
0.4
0.3
0.2
0.1
0.0
2.4
2.6
2.8
3.0
Z'(Ω·cm2)

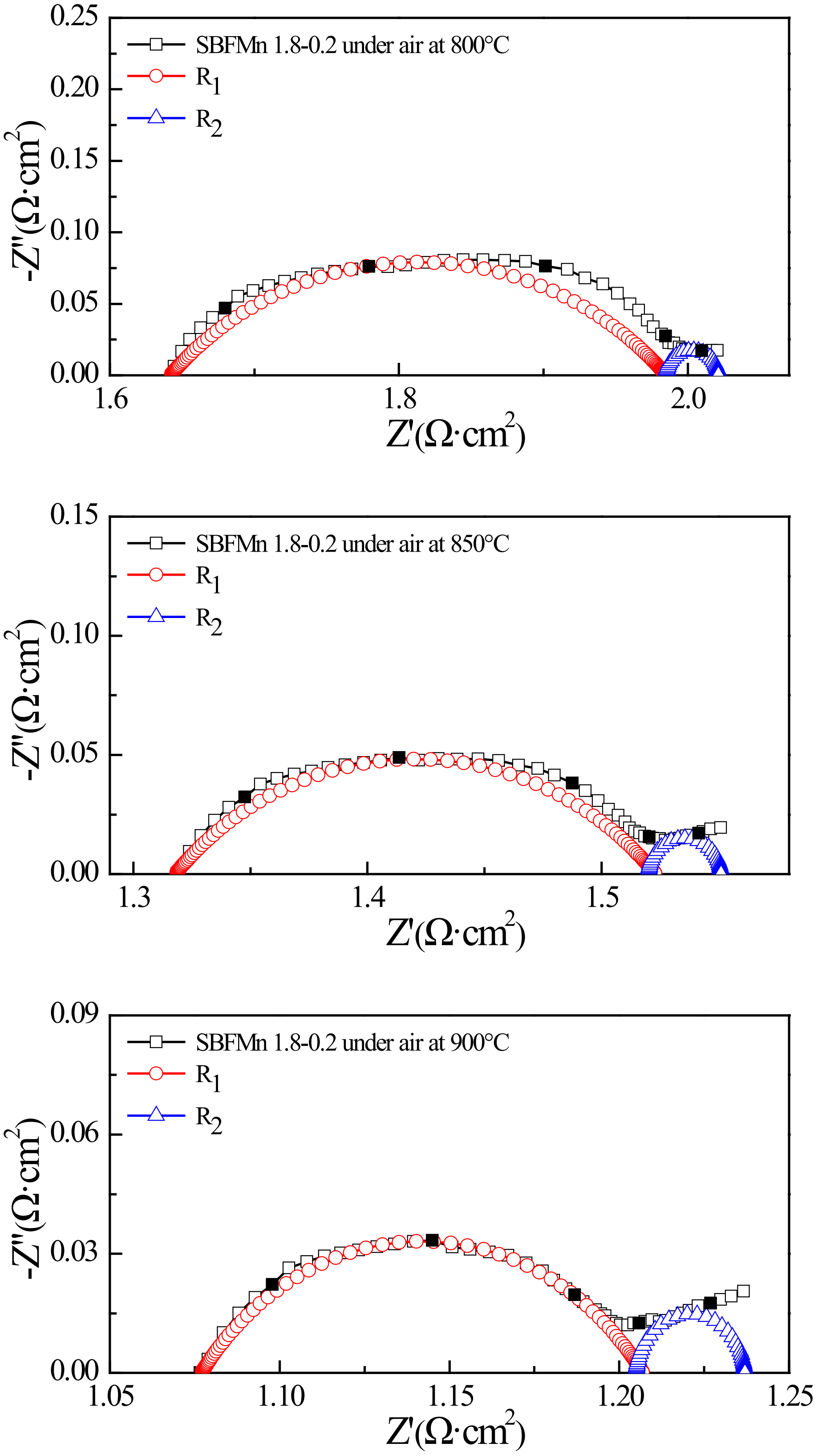
SBFMn 1.8-0.2 under air at 800°C
R1
R2
-Z''(Ω·cm²)
0.25
0.20
0.15
0.10
0.05
0.00
Z'(Ω·cm²)
1.6
1.8
2.0
SBFMn 1.8-0.2 under air at 850°C
R1
R2
-Z''(Ω·cm²)
0.15
0.10
0.05
0.00
Z'(Ω·cm²)
1.3
1.4
1.5
SBFMn 1.8-0.2 under air at 900°C
R1
R2
-Z''(Ω·cm²)
0.09
0.06
0.03
0.00
Z'(Ω·cm²)
1.05
1.10
1.15
1.20
1.25

(a)

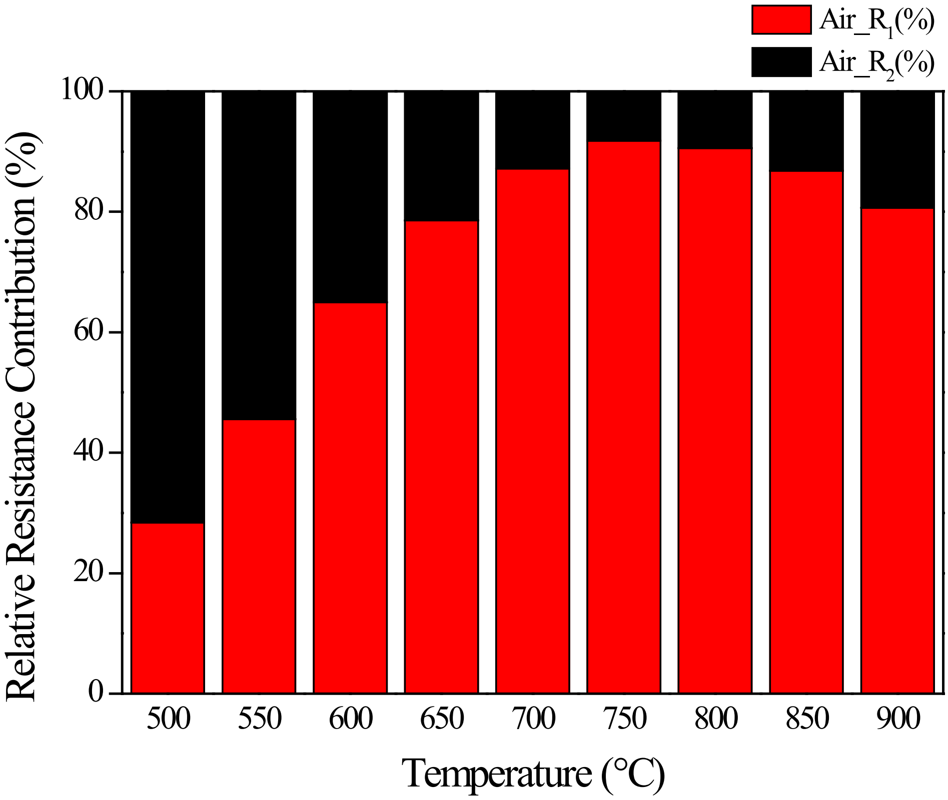
Air_R1(%)
Air_R2(%)
Relative Resistance Contribution (%)
100
80
60
40
20
0
500
550
600
650
700
750
800
850
900
Temperature (°C)

(b)

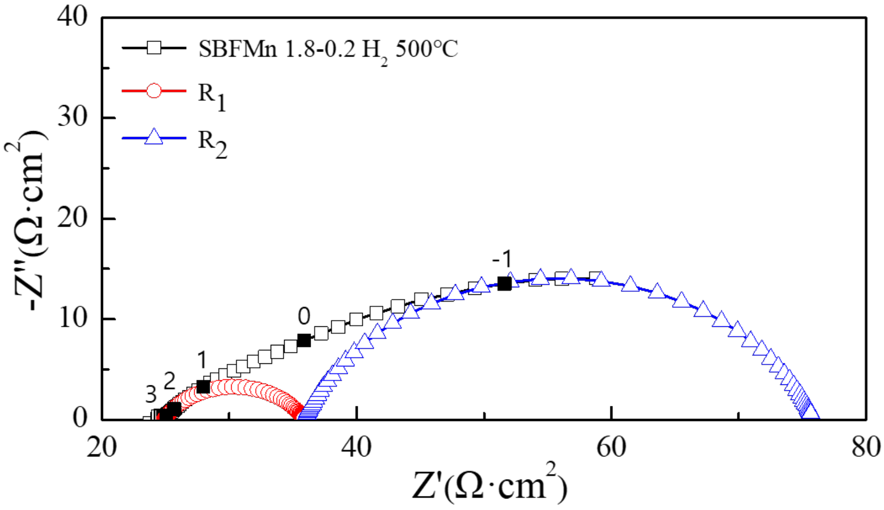
SBFMn 1.8-0.2 H2 500°C
R1
R2
-Z''(Ω·cm2)
Z'(Ω·cm2)
0
10
20
30
40
20
40
60
80
3
2
1
0
-1

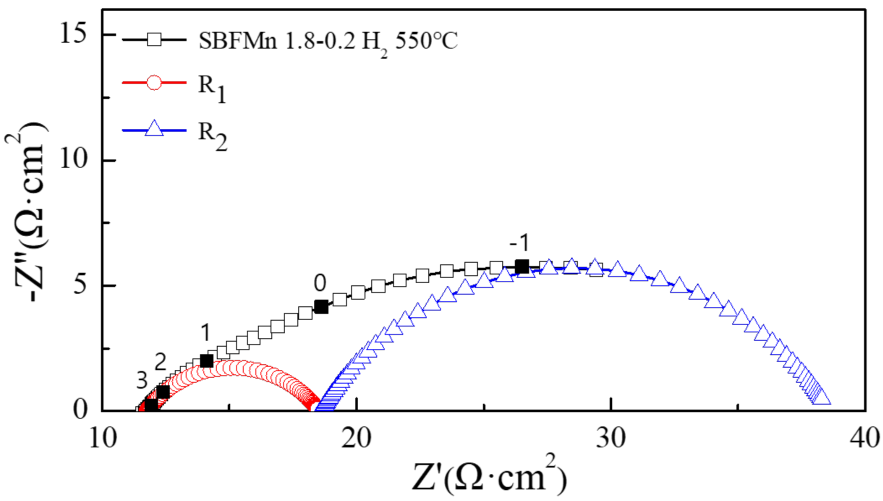
SBFMn 1.8-0.2 H2 550°C
R1
R2
-Z''(Ω·cm2)
Z'(Ω·cm2)
0
5
10
15
10
20
30
40
3
2
1
0
-1

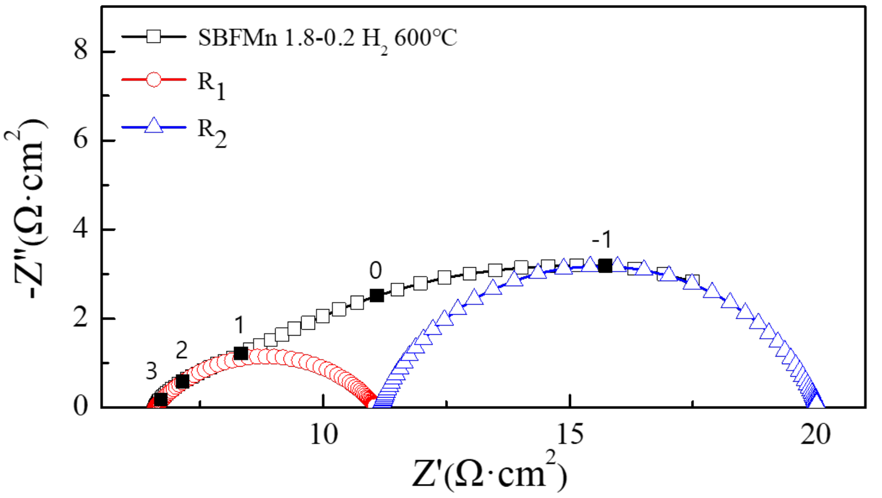
SBFMn 1.8-0.2 H2 600°C
R1
R2
-Z''(Ω·cm2)
Z'(Ω·cm2)
0
2
4
6
8
10
15
20
3
2
1
0
-1

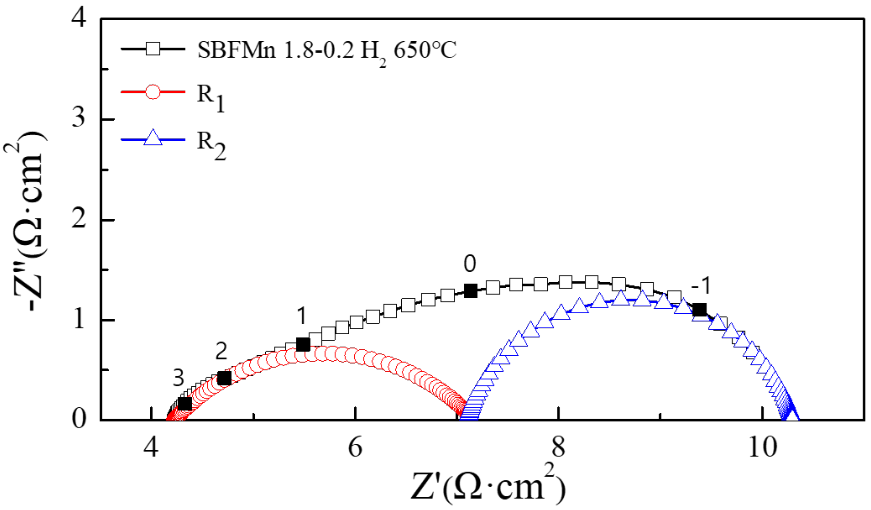
SBFMn 1.8-0.2 H2 650°C
R1
R2
-Z''(Ω·cm2)
Z'(Ω·cm2)
0
1
2
3
4
4
6
8
10
3
2
1
0
-1

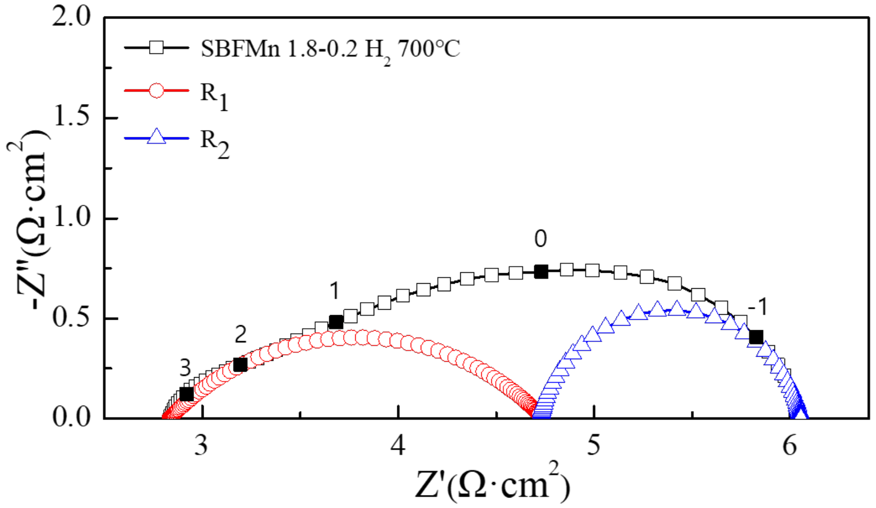
SBFMn 1.8-0.2 H2 700°C
R1
R2
-Z''(Ω·cm2)
Z'(Ω·cm2)
0.0
0.5
1.0
1.5
2.0
3
4
5
6
3
2
1
0
-1

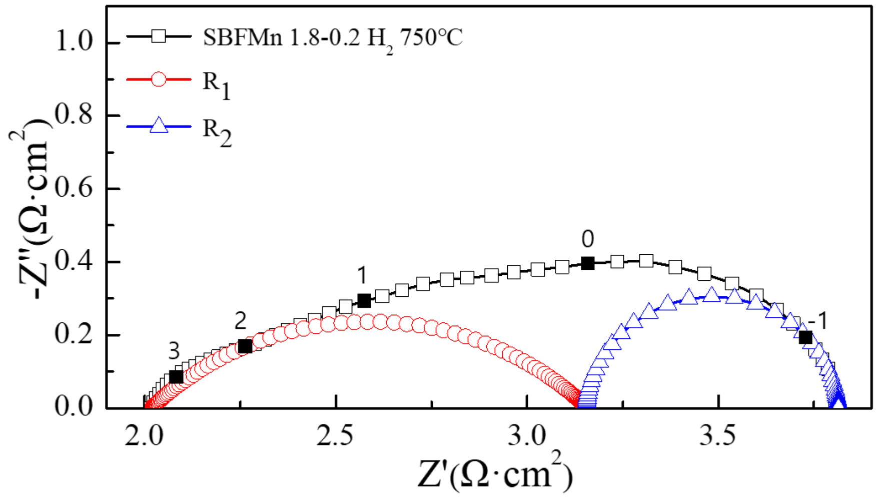
SBFMn 1.8-0.2 H2 750°C
R1
R2
-Z''(Ω·cm2)
Z'(Ω·cm2)
0.0
0.2
0.4
0.6
0.8
1.0
2.0
2.5
3.0
3.5
3
2
1
0
-1

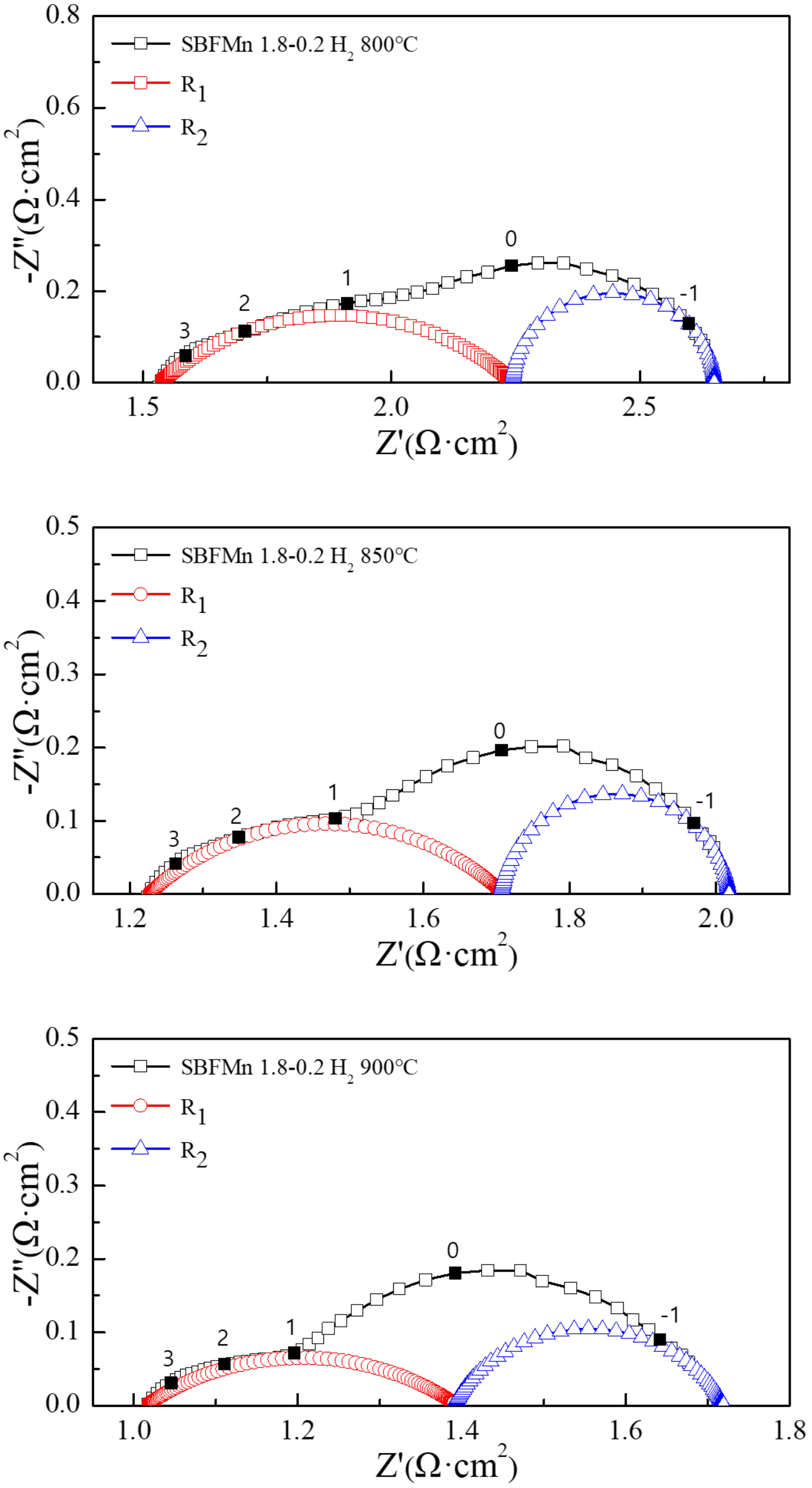
SBFMn 1.8-0.2 H$_2$ 800°C
R$_1$
R$_2$
-Z''(Ω·cm$^2$)
Z'(Ω·cm$^2$)
0.0
0.2
0.4
0.6
0.8
1.5
2.0
2.5
3
2
1
0
-1
SBFMn 1.8-0.2 H$_2$ 850°C
R$_1$
R$_2$
-Z''(Ω·cm$^2$)
Z'(Ω·cm$^2$)
0.0
0.1
0.2
0.3
0.4
0.5
1.2
1.4
1.6
1.8
2.0
3
2
1
0
-1
SBFMn 1.8-0.2 H$_2$ 900°C
R$_1$
R$_2$
-Z''(Ω·cm$^2$)
Z'(Ω·cm$^2$)
0.0
0.1
0.2
0.3
0.4
0.5
1.0
1.2
1.4
1.6
1.8
3
2
1
0
-1

(c)

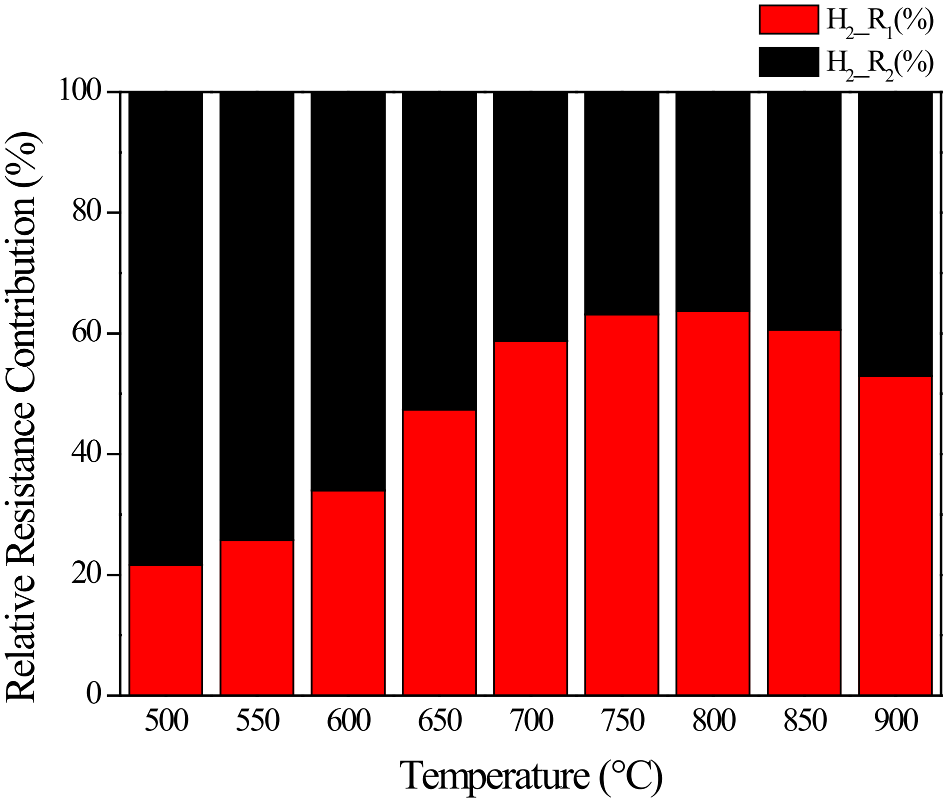

(d)

Fig 4. Impedance characteristics and resistance behavior of SBFMn 1.8-0.2 composition at different temperatures. (a) Impedance plots measured in air, (b) Temperature dependence of $R_1$ and $R_2$ components in air, (c) Impedance plots measured in hydrogen atmosphere, (d) Temperature dependence of $R_1$ and $R_2$ components in hydrogen atmosphere

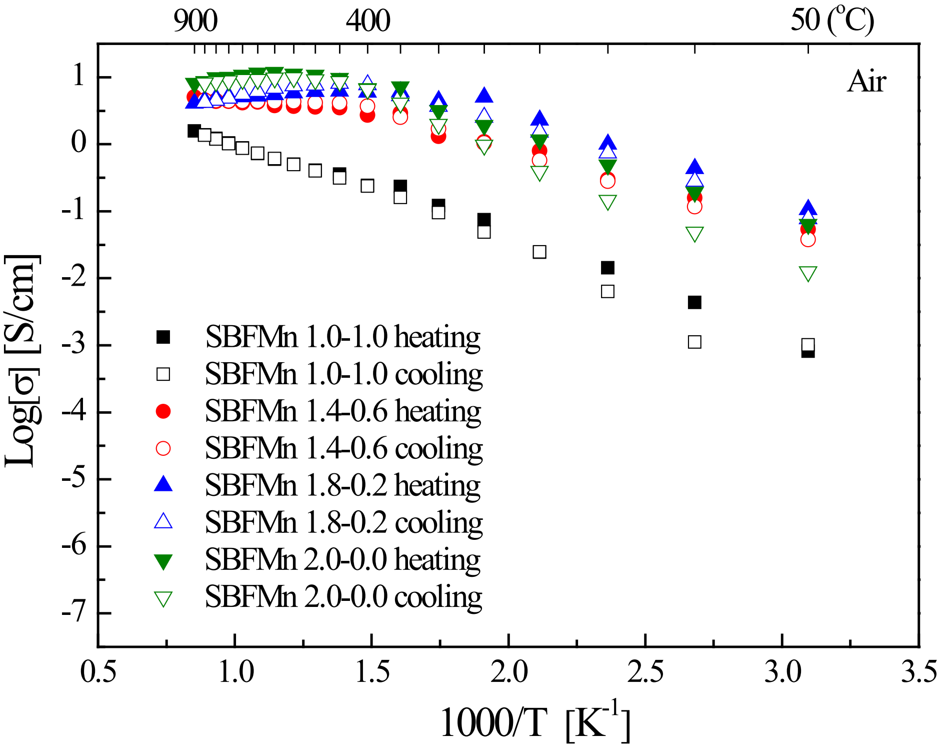
900
400
50 (°C)
Air
Log[σ] [S/cm]
1
0
-1
-2
-3
-4
-5
-6
-7
0.5
1.0
1.5
2.0
2.5
3.0
3.5
1000/T [K$^{-1}$]
■ SBFMn 1.0-1.0 heating
□ SBFMn 1.0-1.0 cooling
● SBFMn 1.4-0.6 heating
○ SBFMn 1.4-0.6 cooling
▲ SBFMn 1.8-0.2 heating
△ SBFMn 1.8-0.2 cooling
▼ SBFMn 2.0-0.0 heating
▽ SBFMn 2.0-0.0 cooling

(a)

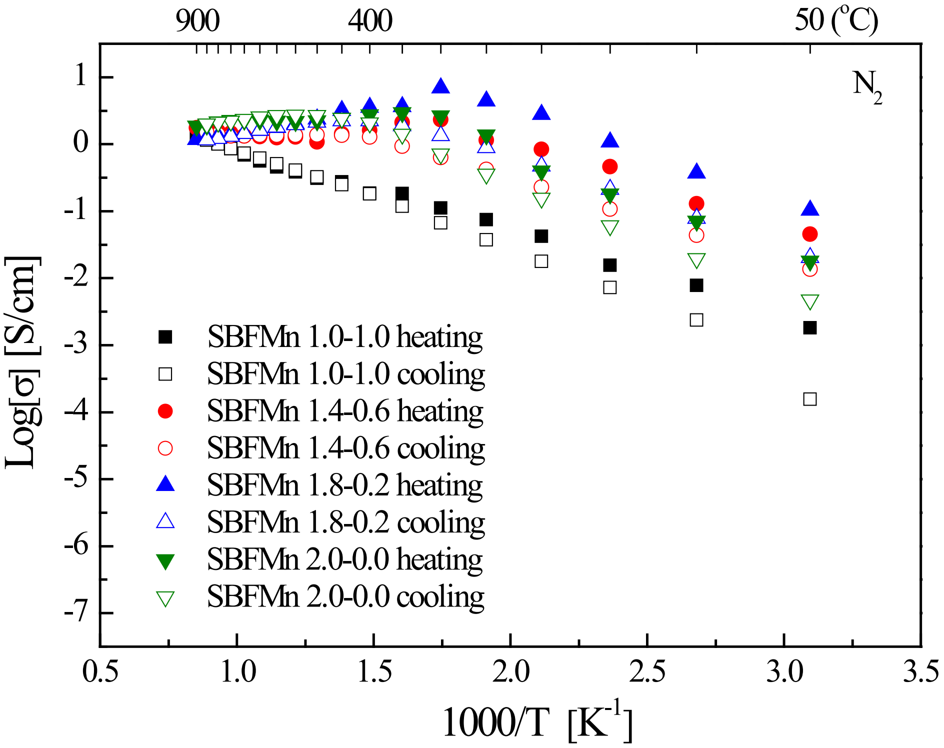
900
400
50 (°C)
N₂
1
0
-1
-2
-3
-4
-5
-6
-7
Log[σ] [S/cm]
0.5
1.0
1.5
2.0
2.5
3.0
3.5
1000/T [K⁻¹]
SBFMn 1.0-1.0 heating
SBFMn 1.0-1.0 cooling
SBFMn 1.4-0.6 heating
SBFMn 1.4-0.6 cooling
SBFMn 1.8-0.2 heating
SBFMn 1.8-0.2 cooling
SBFMn 2.0-0.0 heating
SBFMn 2.0-0.0 cooling

(b)

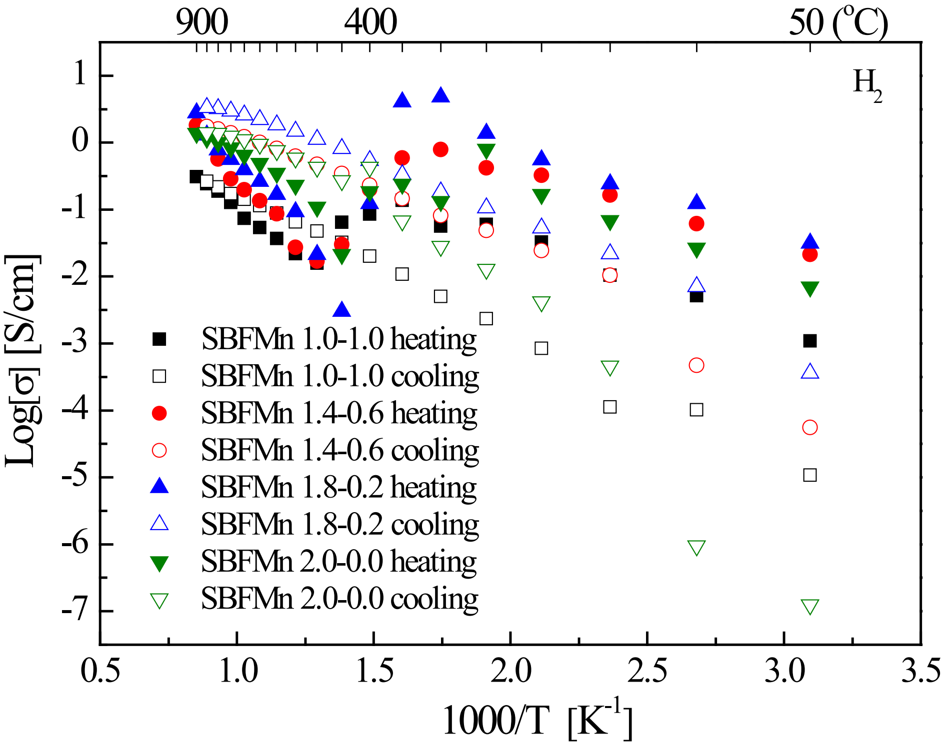

(c)

Fig 5. Electrical conductivity of SBFMn measured under (a) air, (b) nitrogen, and (c) hydrogen atmospheres

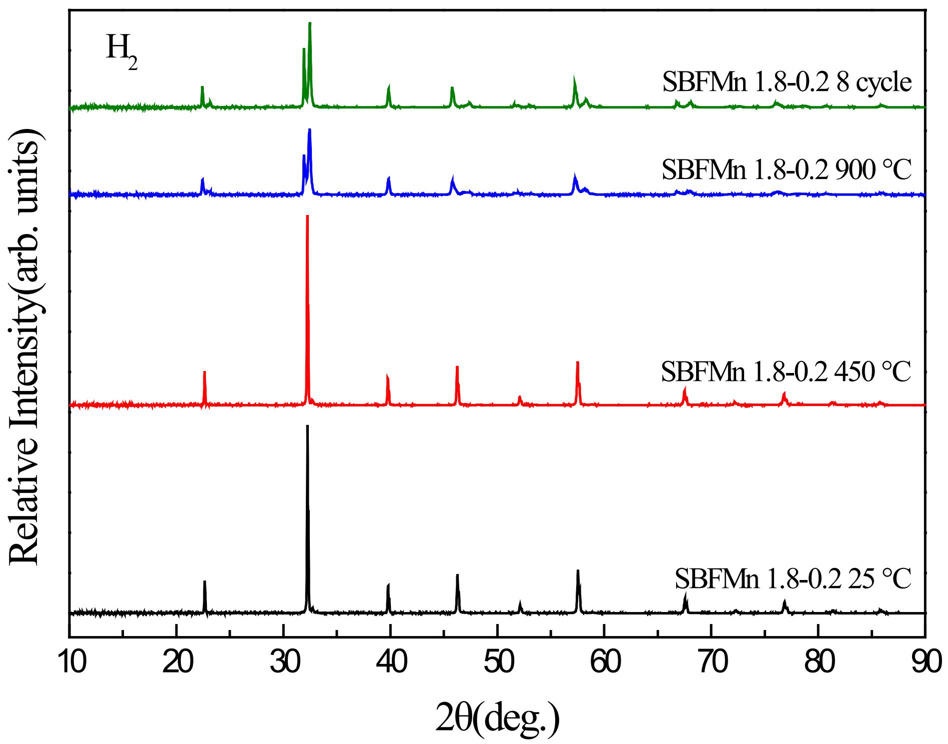
H$_2$
SBFMn 1.8-0.2 8 cycle
SBFMn 1.8-0.2 900 °C
SBFMn 1.8-0.2 450 °C
SBFMn 1.8-0.2 25 °C
Relative Intensity(arb. units)
2θ(deg.)
10
20
30
40
50
60
70
80
90

(a)

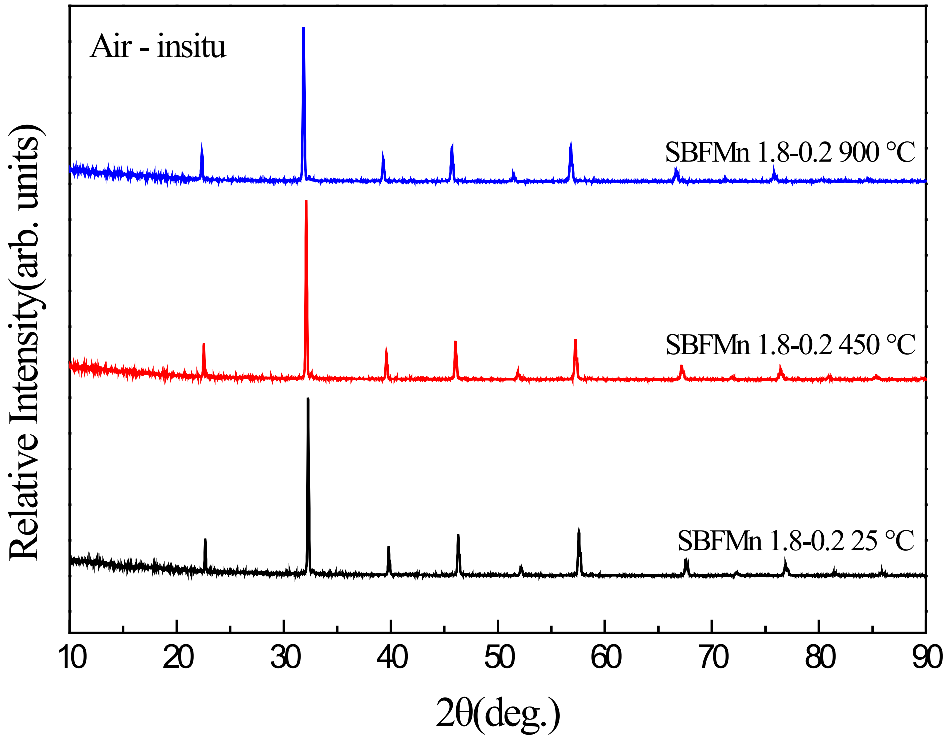

(b)

Fig 6. XRD patterns of SBFMn 1.8-0.2 samples : after heat treatment at 25 °C, 450 °C, and 900 °C (a) in hydrogen atmosphere and ex-situ measurement, and measured (b) in situ under air atmosphere at corresponding temperature

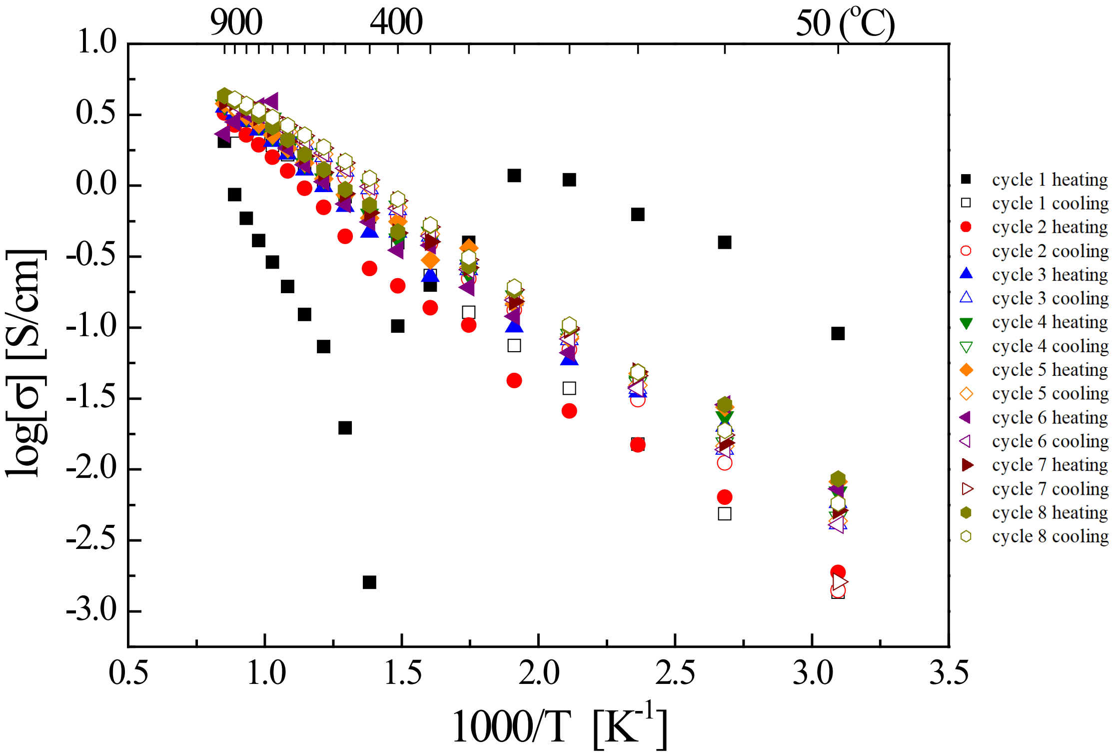

Fig 7. Electrical conductivity of SBFMn 1.8-0.2 under hydrogen atmosphere over 8 thermal cycles

Table 1. Sample abbreviation

| | **x** | **Composition** | **Abbreviation** |
|---|---|---|---|
| SBFMn oxide systems | 0.0 | $SmBaFe_2O_{5+d}$ | SBFMn 2.0-0.0 |
| | 0.1 | $SmBa(Fe_{0.9}Mn_{0.1})_2O_{5+d}$ | SBFMn 1.8-0.2 |
| | 0.3 | $SmBa(Fe_{0.7}Mn_{0.3})_2O_{5+d}$ | SBFMn 1.4-0.6 |
| | 0.5 | $SmBa(Fe_{0.5}Mn_{0.5})_2O_{5+d}$ | SBFMn 1.0-1.0 |

Table 2. ASR of SBFMn 1.8–0.2 electrode in air and hydrogen atmospheres

| Resistance ($\Omega cm^2$) | | | | | | |
|---|---|---|---|---|---|---|
| Temp (℃) | Air | | | $H_2$ | | |
| | $R_1$ | $R_2$ | $R_p$ | $R_1$ | $R_2$ | $R_p$ |
| 500 | 3.650 | 9.194 | 12.844 | 4.317 | 15.608 | 19.926 |
| 550 | 2.099 | 2.510 | 4.610 | 2.688 | 7.730 | 10.418 |
| 600 | 1.236 | 0.667 | 1.903 | 1.791 | 3.480 | 5.271 |
| 650 | 0.704 | 0.192 | 0.896 | 1.129 | 1.254 | 2.384 |
| 700 | 0.394 | 0.058 | 0.452 | 0.742 | 0.521 | 1.263 |
| 750 | 0.213 | 0.019 | 0.232 | 0.444 | 0.259 | 0.703 |
| 800 | 0.134 | 0.014 | 0.148 | 0.277 | 0.158 | 0.436 |
| 850 | 0.079 | 0.012 | 0.091 | 0.188 | 0.122 | 0.310 |
| 900 | 0.050 | 0.012 | 0.062 | 0.145 | 0.129 | 0.275 |